SANDIA REPORT

SAND2013-8084
Unlimited Release
Printed September 2013

Final LDRD Report: Nanoscale Mechanisms in Advanced Aging of Materials During Storage of Spent "High Burnup" Nuclear Fuel

Blythe G. Clark, Shreyas Rajasekhara, David Enos, Remi Dingreville, Barney L. Doyle, Khalid Hattar, and Ruth Weiner

Prepared by
Sandia National Laboratories
Albuquerque, New Mexico 87185 and Livermore, California 94550

Sandia National Laboratories is a multi-program laboratory managed and operated by Sandia Corporation, a wholly owned subsidiary of Lockheed Martin Corporation, for the U.S. Department of Energy's National Nuclear Security Administration under contract DE-AC04-94AL85000.

Approved for public release; further dissemination unlimited.

Issued by Sandia National Laboratories, operated for the United States Department of Energy by Sandia Corporation.

NOTICE: This report was prepared as an account of work sponsored by an agency of the United States Government. Neither the United States Government, nor any agency thereof, nor any of their employees, nor any of their contractors, subcontractors, or their employees, make any warranty, express or implied, or assume any legal liability or responsibility for the accuracy, completeness, or usefulness of any information, apparatus, product, or process disclosed, or represent that its use would not infringe privately owned rights. Reference herein to any specific commercial product, process, or service by trade name, trademark, manufacturer, or otherwise, does not necessarily constitute or imply its endorsement, recommendation, or favoring by the United States Government, any agency thereof, or any of their contractors or subcontractors. The views and opinions expressed herein do not necessarily state or reflect those of the United States Government, any agency thereof, or any of their contractors.

Printed in the United States of America. This report has been reproduced directly from the best available copy.

Available to DOE and DOE contractors from
U.S. Department of Energy
Office of Scientific and Technical Information
P.O. Box 62
Oak Ridge, TN 37831

Telephone: (865) 576-8401
Facsimile: (865) 576-5728
E-Mail: reports@adonis.osti.gov
Online ordering: http://www.osti.gov/bridge

Available to the public from
U.S. Department of Commerce
National Technical Information Service
5285 Port Royal Rd.
Springfield, VA 22161

Telephone: (800) 553-6847
Facsimile: (703) 605-6900
E-Mail: orders@ntis.fedworld.gov
Online order: http://www.ntis.gov/help/ordermethods.asp?loc=7-4-0#online

SAND2013-8084
Unlimited Release
Printed September 2013

Final LDRD Report: Nanoscale Mechanisms in Advanced Aging of Materials During Storage of Spent "High Burnup" Nuclear Fuel

Blythe G. Clark[1], Shreyas Rajasekhara[1], David Enos[2], Remi Dingreville[3], Barney Doyle[1], Khalid Hattar[1], and Ruth Weiner[4]

[1]Radiation-Solid Interactions, [2]Materials Reliability, [3]Structural & Thermal Analysis, and [4]Risk & Reliability Analysis Departments

Sandia National Laboratories
P.O. Box 5800
Albuquerque, New Mexico 87185-MS1423

Abstract

We present the results of a three-year LDRD project focused on understanding microstructural evolution and related property changes in Zr-based nuclear cladding materials towards the development of high fidelity predictive simulations for long term dry storage. Experiments and modeling efforts have focused on the effects of hydride formation and accumulation of irradiation defects. Key results include: determination of the influence of composition and defect structures on hydride formation; measurement of the electrochemical property differences between hydride and parent material for understanding and predicting corrosion resistance; *in situ* environmental transmission electron microscope observation of hydride formation; development of a predictive simulation for mechanical property changes as a function of irradiation dose; novel test method development for microtensile testing of ion-irradiated material to simulate the effect of neutron irradiation on mechanical properties; and successful demonstration of an Idaho National Labs-based sample preparation and shipping method for subsequent Sandia-based analysis of post-reactor cladding.

ACKNOWLEDGMENTS

The authors gratefully acknowledge Stuart van Deusen and Dan Buller for ion beam irradiation support, Jim Banks for elastic recoil detection assistance, Garry Bryant, Michael Rye, and Lisa Lowery for TEM sample preparation, Paul Kotula for energy dispersive x-ray analysis, Brad Salzbrenner and Brad Boyce for mechanical testing, Mike Marshall, Lysle Serna, and Mike Martinez for assistance with microtensile sample preparation, Dick Grant for microprobe analysis, Mark Rodriguez and Jamie Griego for X-ray analysis, Bailey Risteen for electrochemical experiment support, Ed Stech (University of Notre Dame) for ion irradiation and implantation of microtensile samples, Melissa Teague (Idaho National Labs) for preparation and shipment of post-reactor cladding samples, and Veena Tikare, S.J. Zinkle (Oak Ridge National Laboratory), T.J. Bartel, and C. Sallaberry for many useful discussions. In addition, we appreciate the support of managers Rick McCormick (project manager), Dave Sandison (former project manager), and Jon Custer throughout this work. This work was funded under LDRD Project Number151328 and Title "Nanoscale Mechanisms in Advanced Aging of Materials During Storage of Spent "High Burnup" Nuclear Fuel".

CONTENTS

FIGURES

TABLES

NOMENCLATURE

ADF	Annular Dark Field
BWR	Boiling Water Reactor
CRUD	Chalk River Unidentified Deposits
EDX	Energy Dispersive X-Ray
ERD	Elastic Recoil Detection
FCC	Face Centered Cubic
FIB	Focused Ion Beam
GwD/MTU	Gigawatt Days per Metric Ton Uranium
HCP	Hexagonal Close Packed
INL	Idaho National Laboratories
LDRD	Lab Directed Research and Development
LWR	Light Water Reactor
OFHC	Oxygen-Free High thermal Conductivity
PWR	Pressurized Water Reactor
RBS	Rutherford Backscattering Spectrometry
SNL	Sandia National Laboratories
STEM	Scanning Transmission Electron Microscope
TEM	Transmission Electron Microscope
US	United States
Zr-2	Zircaloy-2
Zr-4	Zircaloy-4

1. INTRODUCTION

The decision to not pursue Yucca Mountain as a nuclear waste repository implies that spent nuclear fuel will have to be stored in a retrievable condition (with claddings maintaining necessary strength and ductility) for an indeterminate amount of time, conceivably on the order of centuries. Compounding this issue is the trend to discharge nuclear fuel after "high burnup", i.e. >45 GWd/MTU. Although the US has >25 years experience in storage of low burnup fuel, there is no precedent for storage of high burnup fuel, where increased radiation dose, hydrogen uptake, and corrosive processes can significantly influence the mechanical properties of the cladding. Current efforts to model the degradation of claddings during interim storage rely heavily on empirical equations, limiting their capacity for long time scale extrapolation. To provide fidelity in the ability to retrieve used fuel from storage either for transportation or further processing, extrapolative, physics-based models must be developed that can predict integrity of the cladding. The goal of this work was to understand the degradation mechanisms in claddings during high burnup and in dry storage for development of high fidelity, predictive models.

2. CHALLENGES FOR LONG TERM DRY STORAGE

Successful licensing and ensured safety of long term dry storage requires knowledge of material degradation mechanisms, such that there is confidence in knowing the state of the fuel assemblies after an extended period of time. For emphasis, a 2002 IAEA report [1] stated the following:

> *It is necessary to provide sufficient evidence that the spent fuel condition will not deteriorate during storage to such an extent that any subsequent handling of the fuel would be prevented or become more difficult, or result in non-compliance with nuclear and radiation protection limits.*

As the cladding that encloses the fuel is considered a ‘last line of defense’ to radioactive material release, there has been significant focus on the need for a better understanding of mechanical property changes in the cladding in-reactor and during dry storage. However, the situation is extremely complex due to the broad range of variables that influence the state of the cladding, for example:

- There are multiple cladding alloys currently in use in the US
- Cladding microstructures and textures are dependent on the processing routes of the supplier
- The neutron dose, swelling, and temperature experienced by the cladding is related to position of the fuel rod within the assembly, and additionally varies along the length of the rod
- The temperatures, pressures, and water chemistry are further dependent on the specific reactor type, e.g. BWR versus PWR
- The temperature profile experienced by the cladding during dry storage is determined by the amount of burn up the assembly experienced in service, as well as the amount of time the assembly spent cooling in on-site pool storage

Because of the breadth of potential mechanical property degradation mechanisms, this LDRD chose to focus on two key aspects: (1) Hydride formation in Zr-based cladding [Section 3], and (2) Effect of Irradiation Damage [Section 4]. Work is further segmented by particular topics of research; each of the segments has its own introduction, results, conclusion, and references for that portion of the work.

1. *Long term storage of spent nuclear fuel – Survey and recommendations*, International Atomic Energy Agency, IAEA-TECDOC-1293, May 2002, pp. 1-108.

3. HYDRIDE FORMATION IN ZR-BASED CLADDING

3.1. Hydrogen Uptake in Zr-2 Studied via ERD

In order to quantify the amount of hydride formed in our experiments, this LDRD pursued the use of Elastic Recoil Detection to obtain depth dependent profiles of hydrogen. The results were compared and verified using cross-sectional TEM analysis. Details of the ERD method can be found in Appendix A. Results of this study were published in: S. Rajasekhara, B. L. Doyle, D. G. Enos, and B. G. Clark, "*Hydrogen uptake in Zircaloy-2 reactor fuel claddings studied with elastic recoil detection*," AIP Conf. Proc. 1524 (2012), pp. 270-275, Conference on Application of Accelerators in Research and Industry (CAARI) 2012.

3.1.1. Introduction & Approach

In modern light water nuclear reactors, Zr-based alloy cladding tubes experience a significant uptake of hydrogen into the cladding due to corrosion at the cladding/water interface [1], [2]. Hydrogen in excess of terminal solid solution solubility in Zr precipitates out as hydrides. When initially formed, these hydrides tend to be oriented circumferentially within the cladding. While the presence of circumferential hydrides does not result in a significant reduction in mechanical strength of the cladding and is not a reason for concern, their re-orientation into radial hydrides during drying and dry storage of the discharged spent nuclear fuel rods diminishes mechanical properties and adversely impacts the structural integrity of the cladding [3], [4].

In order to further understand the kinetics of hydride formation, characterization of hydrogen uptake in a typical Zr-based cladding material was performed. Zr-2 samples were electrolytically charged with hydrogen and subsequently analyzed with ERD and TEM. Hydrogen charging *via* an electrolytic route was employed because the charging conditions may be controlled, and very high hydrogen fugacities may be achieved [5]. This was accomplished at a current density of 100 mA/cm2 in a 90C, 0.1M sulfuric acid solution. ERD is an ideal technique for depth-profiling light elements such as hydrogen [6]. In addition, ERD and related ion beam techniques have been employed to examine hydrogen ingress into oxide layers on Zr [7], and electrochemical oxidation of Zr cladding [8]. Details of the ERD method are included in Appendix A. TEM was performed with a Philips CM30 operated at 300 keV.

3.1.2. Results Summary

For data acquired with He ERD, concentration profiles as a function of charging times are shown in Figure 1a. The depth of hydrogen profiles as well as the peak of hydrogen concentration increased with charging times. For the longest charging duration, the peak of hydrogen profile plateaued at a value of approximately 66 at%, which is consistent with the formation of a ZrH_2. The equivalent thickness of ZrH_2 was plotted as a function of time on a log-log scale yielding a power law relationship $d_{eq} \sim At^b$ with $b \sim ½$ (Figure 1), implying that the equivalent thickness of ZrH_2 was proportional to the square root of time and that the growth rate of the hydride layer appeared to be controlled by mass transport of hydrogen through the hydride layer to hydride/matrix interface. In order to confirm this result, the Si ERD data was analyzed in a similar fashion and the results were comparable to that obtained by He ERD.

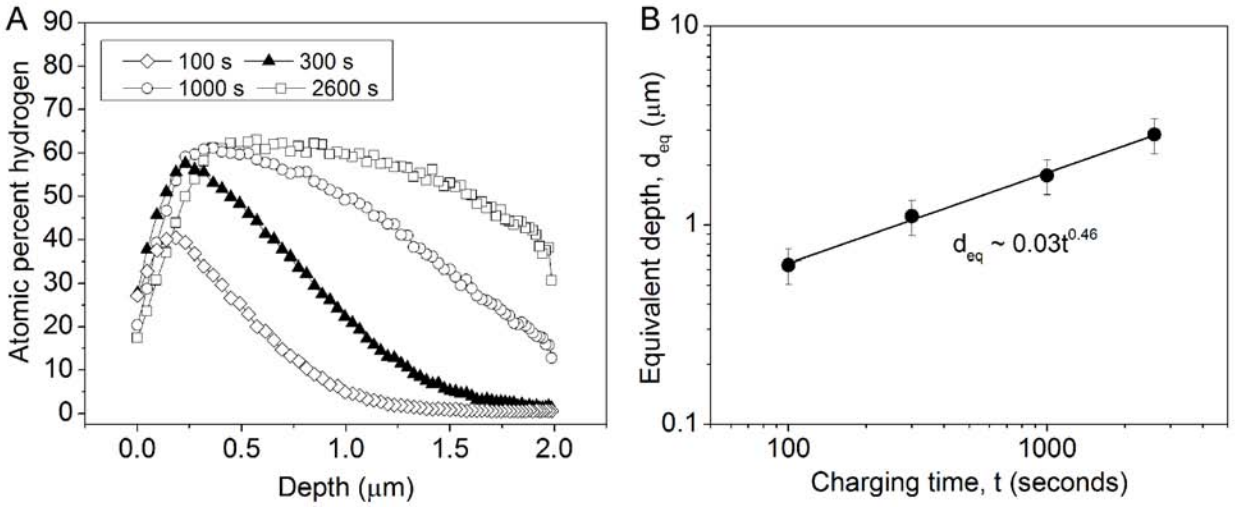

Figure 1. A) Atomic hydrogen concentration as a function of depth for charging times ranging from 100 s to 2,600 s. B) Equivalent depth of ZrH_2, obtained by determining areal densities from concentration profiles shown in (A), as a function of electrolytic charging time.

The nature and extent of hydride formation was confirmed in via cross-sectional TEM imaging of FIB lift-out Zr-2 samples that had been charged for 100, 300, and 1000 s (Figure 2). The bright-field TEM montage image clearly shows a continuous hydride layer that is approximately 100 μm at its narrowest and 1 micron at its widest, and Zr-2 grains of approximately 2 – 5 microns in size in the underlying host matrix. These TEM results indicate that the advancing hydride layer is not completely uniform in thickness. This observation suggests that the equivalent thickness determined by ERD represents an 'average' hydride thickness associated with a given charging.

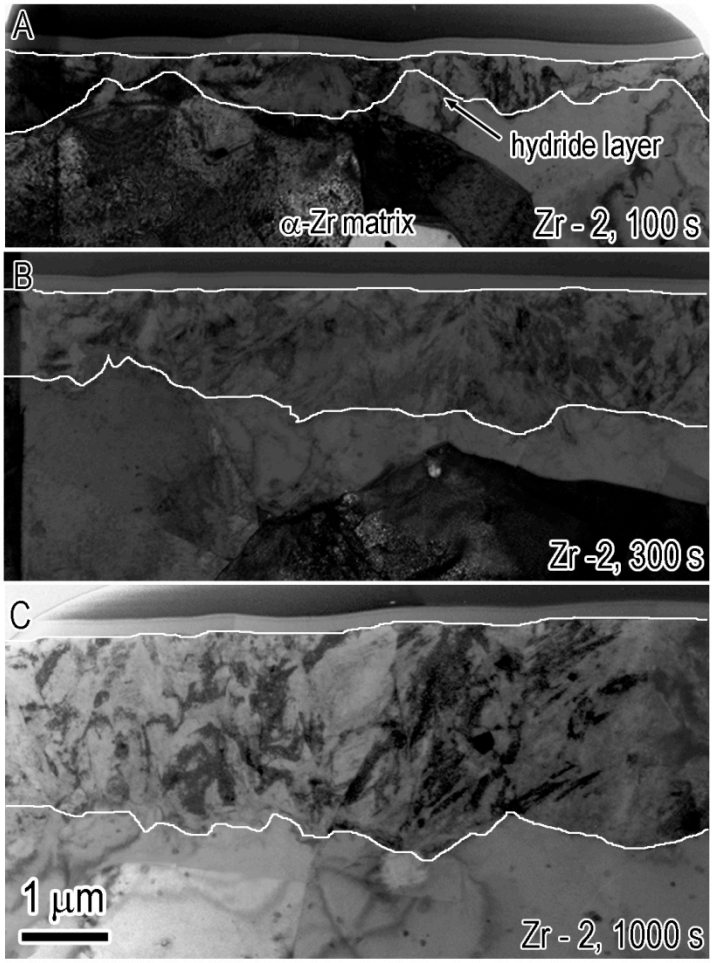

Figure 2. TEM images of Zr-2 FIB-liftouts after aqueous charging for (A) 100 s, (B) 300 s, and (C) 1000 s.

Assuming a diffusion-limited hydrogen ingress, an effective diffusivity of hydrogen in the hydride layer $D_{eff.}^{H}$ was determined from the slope of a linear fit to the equivalent depth vs. time data shown in Fig. 1b and is approximately equal to 4.3×10^{-11} cm^2/s. This value is lower than that reported in the literature for pure α-Zr, however the experiments herein measure hydrogen diffusivity in the hydride layer. Our results are qualitatively consistent with those reported by Kido et al.[9] who showed hydrogen diffusivities in the hydride phase to be substantially lower than that in α-Zr.

3.1.3. Conclusions

Hydrogen uptake and hydride formation in Zircaloy – 2 was probed with ERD and TEM. Compositional data from ERD, coupled with microstructural information obtained through TEM suggest the formation of a ZrH_2 hydride layer. The effective thickness of the hydride layer was approximately proportional to the square root of the charging time, suggesting a diffusion limited hydride layer growth. The effective hydrogen diffusivity value in Zr-2 is significantly lower than those reported in literature, which was attributed to hydrogen diffusion in the hydride layer.

3.1.4. References

1. Motta, A.T., *Waterside corrosion in zirconium alloys.* Journal of Metals, 2011. **63**: p. 59-63.
2. Cox, B., *A mechanism for the hydrogen uptake process in zirconium alloys.* Journal of Nuclear Materials, 1999. **264**: p. 283-294.
3. H. C. Chu, S.K.W., K. F. Chien, R. C. Kuo, *Effect of radial hydrides on the axial and hoop mechanical properties of Zircaloy -4 cladding.* Journal of Nuclear Materials, 2007. **362**: p. 93-103.
4. R. S. Daum, S.M., Y. Liu, M. C. Billone, *Radial-hydride embrittlement of high-burnup Zircaloy -4 fuel cladding.* Journal of Nuclear Science and Technology, 2006. **43**: p. 1054-1067.
5. R. N. Iyer, H.W.P., *Mechanism and kinetics of electrochemical hydrogen entry and degradation of metallic systems.* Annual Review of Materials Science 1990. **20**: p. 299 - 338.
6. J. R. Tesmer, M.N., J. C. Barbour, C. J. Maggiore, J. W. Mayer (eds.), *Handbook of modern ion beam materials analysis*, in *Materials Research Society*. 1995. p. 83-138.
7. D. Khatamian, F.D.M., *An ion beam study of hydrogen diffusion in oxides of Zr and Zr-Nb (2.5 wt%).* Journal of Nuclear Materials, 1989. **166**: p. 300-306.
8. H. J. Whitlow, Y.Z., Y. Wang, T. Winzell, N. Simic, E. Ahlberg, M. Limback, G. Wikmark, *Studies of electrochemical oxidation of Zircaloy nuclear reactor fuel cladding using time-of-flight elastic recoil detection analysis.* Nuclear Instruments and Methods in Physics Research, 2000. **B 161-163**: p. 584-589.
9. T. Kido, M.S., *Development of a method to charge hydrogen into zirconium alloys.* Nihon Genshiryoku Gakkai Wabun Rombunshi, 2002. **1**: p. 469-471.

3.2. Influence of Composition on Hydride Formation

As discussed in Section 2, there are multiple cladding compositions currently in use in the US for light water reactors. The three most common of these are Zr-4, Zr-2 and Zirlo^{TM}; all are Zr-based alloys. Here, we studied the influence of composition on formation of hydride. Complete results are being prepared for publication: S. Rajasekhara, P. G. Kotula, D. G. Enos, B. L. Doyle, and B. G. Clark, "*Influence of Zr-Alloy Composition on Hydride Formation during the Initial Period of Hydrogen Charging*," in preparation for J. of Nuclear Materials.

3.2.1. Introduction & Approach

A lack of permanent solution for storage of used nuclear fuel assemblies requires that above ground dry storage be used for used nuclear fuel storage indefinitely, potentially on the order of centuries [1-3]. The process of transferring spent nuclear fuel assemblies from wet storage pools, where the used nuclear fuel assemblies are typically stored after service, to dry storage

entails a temperature excursion that may dissolve pre-existing circumferential hydrides on the cladding surface into the cladding matrix [4]. Subsequent controlled cooling in dry storage, and the presence of hoop stresses in the cladding could result in re-precipitation of hydrogen as radial hydrides [4-7]. It has been suggested that formation of radial hydrides offers easy pathways for crack propagation and could impact structural integrity of cladding assemblies [5-7]. This phenomenon is a cause for concern not only during storage but also for any subsequent transportation of these assemblies [3, 8, 9]. Since the nuclear regulatory commission requires cladding assemblies in dry storage to have structural integrity, predictive modeling is a viable option to validate this requirement. However, systematic experiments regarding hydride formation in Zr-based cladding alloys as a function of composition, critical to inform such models, are currently lacking. Here we prepared samples from Zr-2, Zr-4, and Zirlo^{TM}, with every effort made to control sample variability such that the only significant difference between samples was composition: samples had comparable texture, grain size, defect structures, and surface treatment prior to aqueous charging. Hydrogen charging of the zirconium alloy samples was accomplished at a current density of 100 mA/cm2 in a 90C, 0.1M sulfuric acid solution. This procedure was selected as it replicated a methodology employed by a number of researchers in the literature [10]. ERD thickness measurements followed the procedure discussed in Appendix A.

3.2.2. Results Summary

Compositions of the three alloys studied, as measured by microprobe analysis, are shown in Table 1. As shown, Zirlo^{TM} has a much higher Nb content in comparison with Zr-2 and Zr-4, and lower Sn and Cr concentrations.

Table 1. Composition of Zircaloy – 2, Zircaloy – 4, and Zirlo^{TM} (in wt %) plate stock coupons determined from electron micro-probe analysis. It is seen that Zirlo^{TM} has substantially lower niobium concentration relative to Zircaloy – 2 and Zircaloy – 4.

	Sn	Nb	Fe	Cr	Ni	Zr
Zircaloy - 2	1.22	0.02	0.17	0.12	0.06	Bal.
Zircaloy - 4	1.20	0.03	0.23	0.13	-	Bal.
Zirlo^{TM}	0.48	1.01	0.11	0.01	-	Bal.

Following aqueous charging for 100, 300, and 1000 s, overall hydride thickness was measured with ERD, as shown in Figure 3. For all alloys, it is seen that the hydride thicknesses increased as a function of charging duration. The hydride thicknesses in Zr-2 and Zr-4 were comparable for all charging durations. In the past, Gulbransen and Andrew [11] have measured weight gain due to hydrogen uptake in Zr-2 for a range of charging durations in a gas-charging experiment. Assuming that a continuous hydride layer was present in their Zr-2 samples, a simple calculation reveals that for identical charging durations and similar charging temperature, hydride thickness obtained by Gulbransen et al. are comparable to that from ERD measurements. This comparison validates ERD as a macroscopic tool to probe hydride thicknesses, and aqueous charging as a reliable means of driving in hydrogen in a controlled fashion. ERD results also showed that the hydride thickness in Zirlo^{TM} was an order of magnitude lower relative to the other two alloys for all of the charging durations.

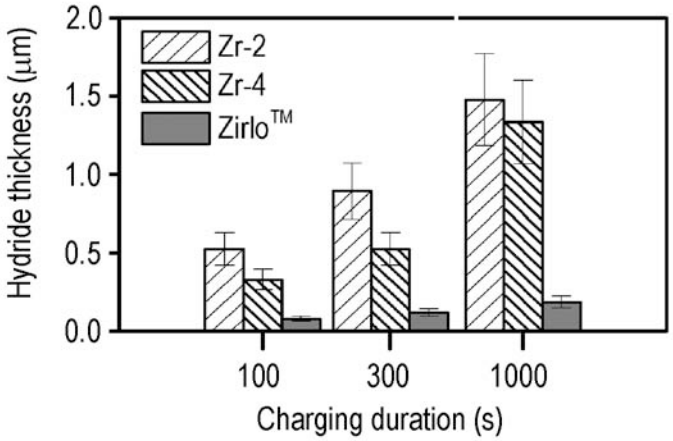

Figure 3. A) Equivalent hydride thicknesses, as a function of charging durations, determined by applying elastic recoil detection on Zircaloy – 2, Zircaloy – 4 and Zirlo™. The hydride thicknesses in Zircaloy – 2 and Zircaloy – 4 are comparable. In contrast, the hydride thickness in Zirlo™ is an order of magnitude smaller relative to Zircaloy – 2 and Zircaloy – 4 for all charging durations.

In order to examine the reason for substantially different hydride thicknesses, electron microscopy studies were performed on Zirlo™ and Zr-2 samples. Bright-field and ADF-STEM images of hydride thicknesses compared well with overall thicknesses obtained by ERD. Further TEM analysis showed that δ-hydride was formed in both alloys, and that in both cases the hydride followed the commonly-observed $\langle 111 \rangle_{\delta-ZrH_{1.6}} // \langle 0001 \rangle_{\alpha-Zr}$ orientation relationship with the matrix. In addition, quantitative microanalysis of the obtained information provided inconclusive evidence that consituents in Zirlo™, e.g. Nb, were segregated or otherwise interacting with the hydride.

3.2.3. Conclusions

In summary, we conducted a controlled study that investigated the impact of alloy composition on hydride formation in polycrystalline Zr-based cladding materials. The key conclusions of this work are:

i) Hydride thickness in Zr – 2 and Zr – 4 were comparable, while Zirlo™ exhibited an order of magnitude lower hydride thickness relative to these alloys, for all charging durations.
ii) The hydride phase in all of these alloys was found to be δ-hydride. The hydride/matrix interface in Zirlo™ and Zr-2 alloys followed a specific orientation relationship with the a-Zr matrix phase, i.e. $\langle 111 \rangle_{\delta-ZrH_{1.6}} // \langle 0001 \rangle_{\alpha-Zr}$. This suggests that the hydride phase and its orientation relationship with the matrix is independent of the alloy composition.
iii) Microanalysis of multiple hydride/matrix interfaces in Zirlo™ was inconclusive to prove that the hydride layer was depleted in Nb. In the absence of conclusive evidence, it is hypothesized alloy composition may impact surface properties, which subsequently impact hydrogen uptake. Further work is required to examine in detail these ideas.

3.2.4. References

1. J. D. Werner, *U. S. Spent Nuclear Fuel Storage*, CRS Report for Congress 7-5700 (2012) 1-57.
2. M. Bunn, J. P. Holdren, A. Macfarlane, S. E. Pickett, A. Suzuki, T. Suzuki, J. Weeks, *Interim Storage of Spent Nuclear Fuel: A Safe, Flexible, and Cost-Effective Near-Term Approach in Spent Fuel Management*, Cambridge MA, Managing the Atom Project, Harvard University, and Project on Socio-technics of Nuclear Energy, University of Tokyo, 2001.
3. M. A. McKinnon, M. E. Cunningham, *Storage Demonstration for High-Burnup Spent Nuclear Fuel - Feasibility Study*, EPRI, Palo Alto, CA, and U. S. Department of Energy, Washington, DC: 2003. 1007872
4. R. S. Daum, S. Majumdar, Y. Liu, M. C. Billone, J. Nucl. Sci. Tech. 43, (2006) 1054-1067.
5. C. K. Chao, K. C. Yang, C. C. Tseng, Nucl. Engg. Des. 238 (2008); 124-129.
6. H. C. Chu, S. K. Wu, K. F. Chien, R. C. Kuo, J. Nucl. Mater. 362 (2007); 93-103
7. M. Aomi, T. Baba, T. Miyashita, K. Kamimura, T. Yasuda, Y. Shinohara, T. Takeda, J. Amer. Soc. Test. Mater. Intl. 5 (2008); 651-671.
8. M. Peehs, J. Fleisch, J. Nucl. Mater. 137 (1986); 190-202.
9. H. Spilker, M. Peehs, H-. P. Dyck, G. Kaspar, K. Nissen, J. Nucl. Mater. 250 (1997); 63-74.
10. E.D. Hindle, G.F. Slattery, "The Influence of Processing Variables on the Grain Structure and Hydride Orientation in Zircaloy-2 Tubing", Journal of the Institute of Metals, Vol. 94 (1966), pp. 245-249.
11. E. A. Gulbransen, K. F. Andrew, J. Electrochem. Soc. 104, (1954) 560-566.

3.3. Electrochemical Properties of Zirconium Hydride

In the previous section, the difference in hydride formation as a function of composition was addressed. This was further explored in cathodic charging experiments where absorption efficiency was analyzed. Complete results are being prepared for publication: D. Enos, B. Risteen, and B. G. Clark, "*The Cathodic Kinetics of Zirconium Alloys and their Hydrides in Acidic Media*," in preparation for J. of the Electrochemical Society.

3.3.1. Introduction & Approach

Hydrogen charging of the zirconium alloy samples was accomplished at a current density of 100 mA/cm2 in a 90C, 0.1M sulfuric acid solution. This procedure was selected as it replicated a methodology employed by a number of researchers in the literature [1]. Despite utilizing nominally identical charging conditions, the efficiency through which hydrogen was absorbed into the metal, in turn forming a hydride, varied with alloy composition. The absorption efficiency as a function of charging time is presented in Figure 4. The efficiency was calculated by comparing the hydrogen required to generate the volume of hydride formed at the metal surface with the total quantity of hydrogen generated at the metal surface. The hydride was assumed to be δ phase ($ZrH_{1.66}$) for the calculation and the hydride layer thickness used was that determined via ERD.

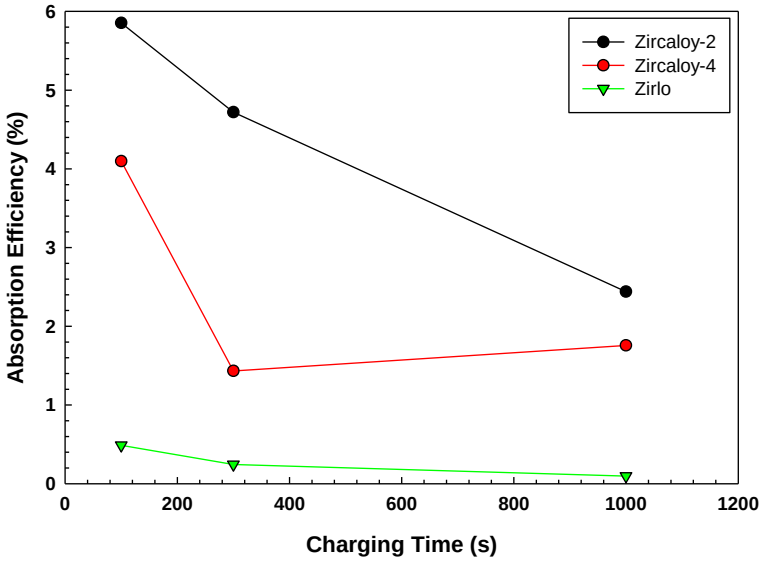

Figure 4. Hydrogen absorption efficiency as a function of charging time and alloy composition.

While the data in the figure is sparse, several clear observations can be made. First, and most obvious, the absorption efficiency (and thus hydride growth rate) is dramatically higher in the two Zircaloys than in Zirlo, consistent with the results presented in Section 3.2. Second, the absorption rate for the two Zircaloys appear to be approaching one another, possibly plateauing at a similar value. This latter observation is not inconsistent with what might be predicted based upon the literature. It has been well established that the hydrogen uptake efficiency is greater for Zircaloy-2 than Zircaloy-4. This has been attributed to the presence of nickel-rich precipitates in the former alloy which are absent in Zircaloy 4. These precipitates are believed to enhance hydrogen uptake [2]. For the samples used to generate Figure 4, the impact of precipitates incident with the metal surface on hydrogen uptake into the bulk of the alloy will be limited as the hydride layer grows. With time, the interface between both Zircaloy 2 and Zircaloy 4 would become nominally identical, being a hydride of similar composition.

One potential explanation for the substantial difference between the Zircaloy alloys and Zirlo would be that the electrochemical behavior of the Zircaloys differed significantly from Zirlo, particularly once hydrided. This could manifest as either altogether different water reduction kinetics on the three alloys, or a change in the electrochemical kinetics upon the covering of the metal surface with a hydride layer created from the underlying alloy. Such changes may be apparent when performing basic electrochemical testing.

A series of electrochemical experiments were performed on Zircaloy-2, Zircaloy-4, and Zirlo specimens to establish if the water reduction kinetics were similar on the three alloys both in the as-received and hydrided condition. Cathodic kinetics were evaluated by performing simple potentiodynamic polarization experiments, scanning from the open circuit/rest potential to potentials well within the water reduction region.

3.3.2. Results Summary

In Figure 5, the cathodic behavior of the three alloys (Zircaloy-2, Zircaloy-4, and Zirlo) are shown. As seen in the figure, the kinetics of the electrochemical reactions occurring on the surface (i.e., the rate, expressed as a current density, as a function of the applied potential (driving force)) differ from alloy to alloy. This is particularly true for small cathodic overpotentials, but becomes less true as the applied potential becomes increasingly large. However, under the conditions used to generate the data in Figure 4, the surface would only be characteristic of the base alloy for early times, until a layer near the surface had been transformed to the hydride phase, at which point the electrochemical behavior of the hydride would dominate. Figure 6 presents similar experiments performed on samples that were cathodically polarized for a period of 1000s, resulting in continuous layer of zirconium hydride on the metal surface. In contrast with the differing behavior of the base alloys, the hydride appears to behave similarly irrespective of the alloy.

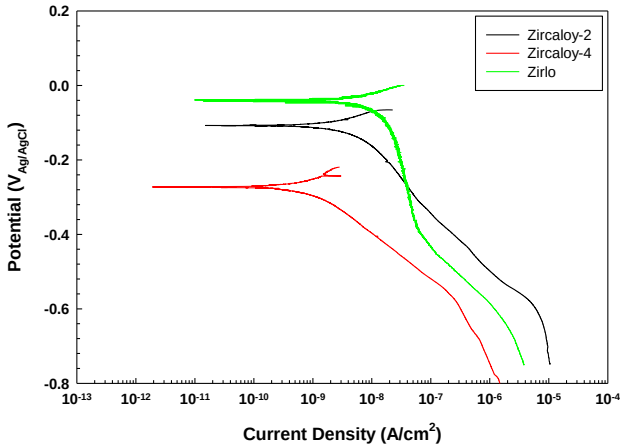

Figure 5. Representative cathodic polarization data for the three alloys explored in this study, illustrating clear differences in the kinetics of the water reduction reaction as a function of applied potential.

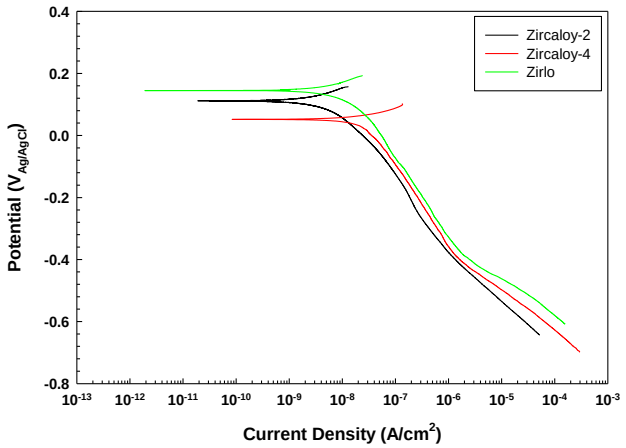

Figure 6. Representative cathodic polarization data for the hydride surfaces of the three alloys explored in this study. In contrast to the base metal, the water reduction kinetics on the hydrides from each alloy were nominally identical as a function of applied potential.

3.3.3. Conclusions

These results strongly suggest that the hydride itself is similar in each material, and thus one might theorize that the adsorption efficiency would also be similar. However, this is clearly not the case as evidenced by the data in Figure 4. One theory offered by Ramasubramanian [3] is that in the Nb containing alloy, the pathway through which hydrogen passes through the oxide is substantially different than in Nb-free alloys, such as Zircaloy-2 or Zircaloy-4. Thus, while the electrochemical generation rate of hydrogen may be similar, the mechanism through which hydrogen is able to pass into the alloy may be more difficult, as evidenced by the substantially lower absorption efficiency observed in this study.

3.3.4. References

1. E.D. Hindle, G.F. Slattery, "The Influence of Processing Variables on the Grain Structure and Hydride Orientation in Zircaloy-2 Tubing", Journal of the Institute of Metals, Vol. 94 (1966), pp. 245-249.
2. B. Cox, P. Rudling, IZNA-1 Special Topics Report – Hydriding Mechanisms and Impact on Fuel Performance, February 2004, Advanced Nuclear Technology, International.
3. N. Ramasubramanian, V. Perovic and M. Leger, Hydrogen Transport in the Oxide and Hydrogen Pickup by the Metal During Out- and In-Reactor Corrosion of Zr2.5Nb Pressure Tube Material, Zirconium in the Nuclear Industry: Twelfth International Symposium, ASTM STP 1354, G. Sabol and G. Moan, Eds. American Society for Testing and Materials, West Conshohocken, PA, 2000, pp. 853-876.

3.4. *In Situ* TEM Observation of Hydride Formation

Sandia's IBL became a beta test site for Protochips environmental cell heating stage in 2011. Because hydrides play such a significant role in determining the mechanical integrity of claddings in dry storage, we wanted to explore the possibility of observing hydride formation during an *in situ* TEM experiment. The results of that effort, discussed below, were presented as a late-breaking poster at the 2012 Microscopy & Microanalysis meeting, and portions were published in: K. Hattar, S. Rajasekhara, B. G. Clark, "In situ *TEM Ion Irradiation and Atmospheric Heating of Cladding Materials*," Mater Res. Soc. Symp. Proc. Vol. 1383, 2012, pp. 61-66.

3.4.1. Introduction & Approach

The mechanical properties of Zr-based nuclear cladding alloys are inherently affected by the presence of Zr hydrides, which are known to embrittle the cladding if oriented along radial directions. Radially-oriented hydrides can be precipitated by a reorientation process when the cladding tubes cool under stress from temperatures at which pre-existing hydrides dissolve into the host matrix [1]. This is of particular concern for fuel assemblies in long term dry storage, where the cladding must maintain its strength and ductility over potentially hundreds of years. The aforementioned precipitation mechanism is highly dependent on the underlying host

microstructure, comprised of grains, precipitates and line defects. In order to develop mesoscale models capable of predicting the structural integrity of nuclear cladding materials during dry storage, a detailed knowledge of the hydride precipitation mechanisms as a function of alloy composition, microstructure, cladding texture, and cooling rates is needed. To date, past studies have employed ex-situ characterization techniques such as optical and transmission electron microscopy (TEM) [2], electron backscatter diffraction [3], and synchrotron X-ray diffraction [4] to examine hydride precipitation in cladding materials. These ex-situ studies have suggested hydrogen uptake and hydride formation depend on (i) hydrogen content [4], (ii) modes of cladding material fabrication [5], (iii) heat treatment procedure [6], and (iv) the presence or absence of stress in the cladding material [7]. However, there remain questions regarding the details of the hydride precipitation mechanisms at the nanoscale that may only be addressed by observing hydride formation in-situ.

In this work, hydride formation in Zirlo^{TM} cladding material was studied using an environmental in-situ heating TEM stage developed by Protochips, Inc. The stage tip holds a gas cell comprised of two Si-based chips with 5 nm thick SiN_x viewing windows, one of which is patterned with a resistive heater, enabling in-situ observation of microstructure evolution during exposure to temperatures up to 1200 ^{o}C and pressures up to 1 atm. The Zirlo^{TM} sample was first prepared using focused ion beam lift out, and then carbon tacked onto the heater-coated SiN_x window of the gas cell. During in-situ observation, hydrogen was introduced and maintained at a pressure of 327 Torr (approximately 0.5 atm, absolute pressure). The temperature was then increased at a rate of 1 °C/s to approximately 400 °C, and held for 90 minutes.

3.4.2. Results Summary

Figure 7A and B show a comparison of the microstructure of the Zirlo^{TM} observed prior to the experiment with that observed in the later stages of annealing. In this comparison, the disappearance of microstructural features (arrow 1) and the formation of a new grain (arrow 2) are evident. The region around the new grain is examined at a higher magnification (Figure 7C) and the analysis of diffraction information acquired from the new grain (Figure 7D) indicates a superimposition of two patterns, one of the parent α-Zr matrix and the other of a face-centered tetragonal phase, consistent with the formation of either ε-ZrH_x ($x > 1.8$) or γ-ZrH.

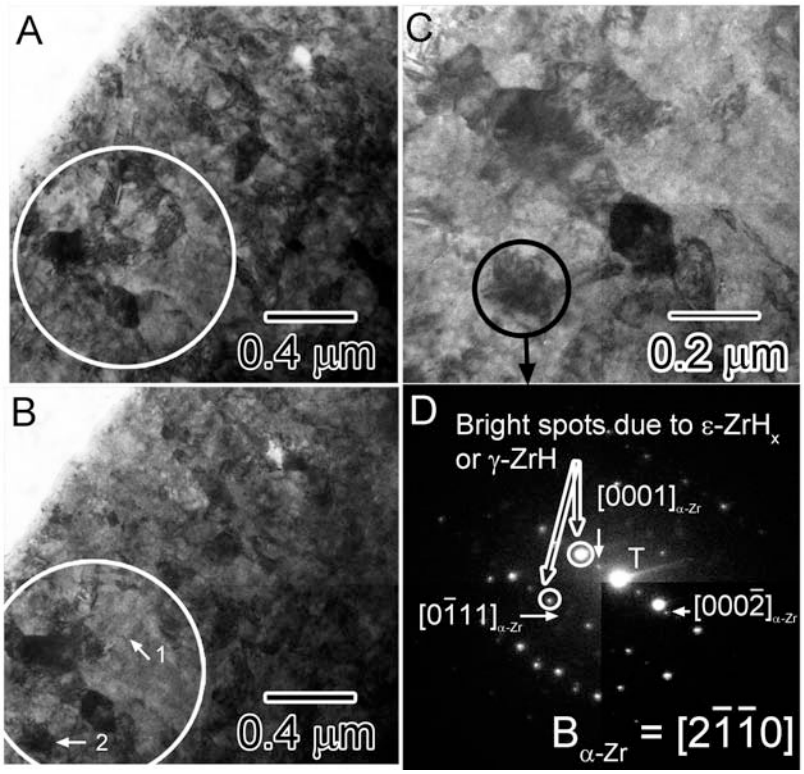

Figure 7. A) and B) Overview of images before the start of in-situ experiment, and after 72 minutes at 400 °C in H_2 atmosphere, C) zoomed-in image of the region of interest around arrow 2 in B) , and D) shows the superimposition of two diffraction patterns obtained from the circled dark grain shown in C), one of the parent α-Zr phase (diffraction spots of weaker intensity) and the other is consistent with a face centered tetragonal hydride phase.

3.4.3. Conclusions

Although further work is required to fully explore the hydride precipitation mechanism, these results show that in-situ environmental heating TEM can be applied to study this mechanism at the nanoscale in order to verify and validate predictive material models. Further experimental results should be pursued in the context of mesoscale models currently being developed, which address reorientation of hydrides and the influence of hydrides on the mechanical properties of Zr-based claddings.

3.4.4. References

1. H. C. Chu, S. K. Wu, R. C. Kuo, *J. Nucl. Mater.* 373 (2008) 319
2. C. E. Ells, *J. Nucl. Mater.* 28 (1968) 129
3. N. A. P. Kiran Kumar, J. A. Szpunar, Z. He, *J. Nucl. Mater.* 403 (2010) 101
4. R. S. Daum, Y. S. Chu, A. T. Motta, *J. Nucl. Mater.* 392 (2009) 453
5. J. J. Kearns, C. R. Woods, *J. Nucl. Mater.* 20 (1966) 241
6. J. S. Bradbrook, G. W. Lorimer, N. Ridley, *J. Nucl. Mater.* 42 (1972) 142
7. D. Hardie, M. W. Shanahan, *J. Nucl. Mater.* 55 (1975) 1

4. EFFECT OF IRRADIATION DAMAGE

4.1. Influence of Irradiation Damage on Hydride Formation

With the current trend to use fuel assemblies within LWRs for longer durations, commonly referred to as high burnup, the cladding materials are experiencing higher levels of neutron irradiation than in the past. Here we studied the effect of increasing levels of irradiation damage on formation of hydride. Complete results are being prepared for publication: S. Rajasekhara, B. L. Doyle, D. G. Enos, K. Hattar, and B.G. Clark, "*Influence of Ion-Irradiation on Hydride Formation in Zircaloy-4*," in preparation for J. of Nuclear Materials.

4.1.1. Introduction & Approach

In the case of high burnup (> 50 GwD/MTU), Zr-based claddings are subjected to higher fluences, higher temperatures, higher hoop stress, and extended corrosion in comparison to the case of low burnup. Understanding the related microstructural changes and their impact on mechanical properties is crucial for predicting cladding behavior after long term dry storage. Of significant interest is understanding how high burnup could impact hydride formation in storage, as hydrides are potentially embrittling if orientated radially within the cladding.

Results from a study by Miyashita et al. in 2006 indicated that hydrogen pick-up rates can dramatically increase in Zr-based claddings at burnups in excess of 35 GwD/MTU [1]. However, it was unclear if this increased hydrogen solubility was due to increased irradiated defect populations, or to flaking of CRUD with extended time in reactor leading to fresh surfaces available for further corrosion.

To determine the influence of irradiated defects on hydrogen uptake, we irradiated Zr-4 coupons with 25 MeV Au ions at Sandia's IBL. These parameters were chosen to produce a fairly uniform defect distribution within the first 1-2 um of material, with Au ions having an end of range implantation depth of approximately 3.5 um according to SRIM calculations [2]. Following preliminary results that suggested a there might be a local temperature rise during irradiation, all ion irradiation was performed with the samples attached to a copper block that was cooled with liquid nitrogen. A thermocouple on the copper block and a feedback circuit was set up to maintain the temperature at 30 °C. Following ion irradiation to 1.5 and 38 dpa, Zr-4 samples were aqueously charged for 1000 s to form hydride, then analyzed via ERD and TEM to measure hydride thickness. ERD details are presented in Appendix A. TEM imaging was performed in a Philips CM30 operated at 300 keV.

4.1.2. Results Summary

Ion irradiated Zr-4 was analyzed via bright-field TEM imaging in the as-irradiated and post-hydride-formation conditions. Figure 8 shows the former, for 1.5 dpa and 38 dpa damage levels. Tilting experiments were performed to confirm that irradiated defects were primarily interstitial loops. In the 1.5 dpa case, these loops were approximately 100 nm in size and were arranged in a dense network throughout the sample. Alternatively, in the 38 dpa case the loops were larger,

150-200 nm in size, and distributed more sparsely within the grains. This suggests that at higher dpas the defect structures have consolidated.

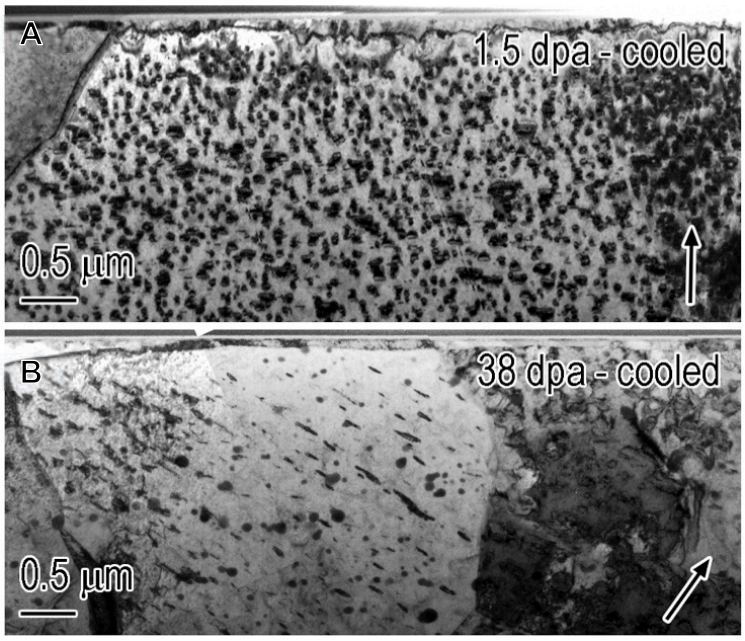

Figure 8. A) Microstructure of the Zr-4 sample ion-irradiated with 25 MeV Au ions to a damage of approximately 1.5 dpa shows a dense network of interstitial loops. B) Ion-irradiation to approximately 38 dpa resulted in a microstructure with a significantly more sparse defect structure. Arrows in A) and B) point towards the g = <0002> vector, which was excited to form a two-beam imaging condition.

Shown in Figure 9a-c are FIB-milled cross sections of hydrided (1000 s charging duraction) Zr-4 with initial damage of 0, 1.5, and 38 dpa. These images were all taken at the same magnification to facilitate comparison, and it is clear that there is a significantly thinner hydride layer in the low damage, 1.5 dpa case in comparison to either the 0 or 38 dpa cases. Figure 9d shows the analogous ERD data for comparison, confirming the TEM observation.

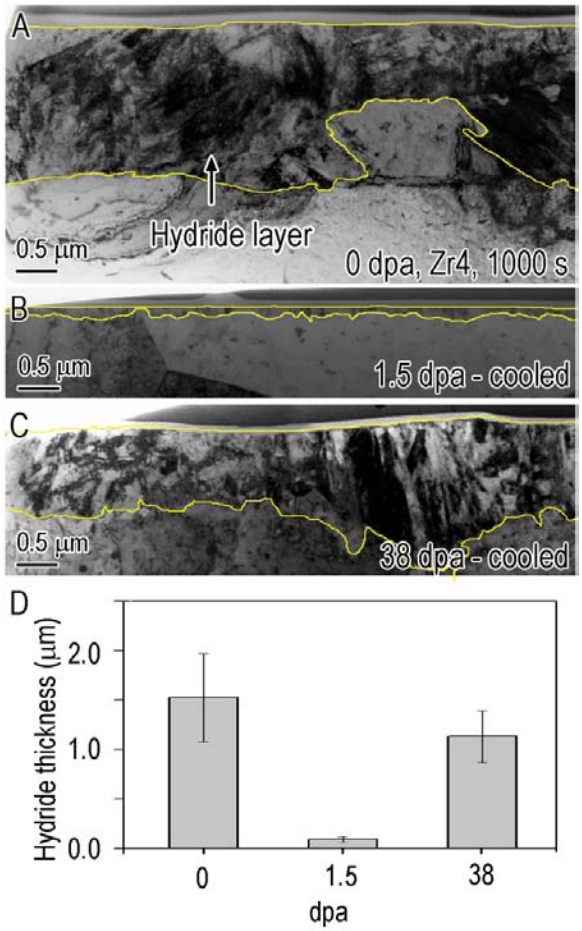

Figure 9. Bright-field TEM images of hydride thickness in Zr-4 following 1000 s of aqueous charging for irradiation damage levels of (A) 0 dpa, (B) 1.5 dpa, and (C) 38 dpa. (D) Hydride thickness data collected via ERD for the three samples.

4.1.3. Conclusions

This work demonstrated an approach to systematically study hydride formation as a function of ion-irradiation dose in Zr-based claddings. In Zr-4 irradiated to 1.5 dpa, interstitial loops were found to be 50-100 nm in diameter and distributed densely through the material. After 1000 s of aqueous charging, a thin ~100 nm layer of hydride was formed. For comparison, unirradiated Zr-4 formed a 1.5 um thick hydride. However, in Zr-4 irradiated to 38 dpa, interstitial loops were 150-200 nm in diameter and distributed more sparsely throughout the material. After aqueously charging the 38 dpa sample for 1000 s, a 1.2 um thick hydride was formed, nearly comparable with that of the unirradiated case.

These results clearly demonstrate an influence of the total irradiation dose and distribution of irradiated defects on the formation of hydride during aqueous charging. We believe that the drastic reduction in hydride thickness observed in the 1.5 dpa case may be due to an interaction of the dislocation loop strain fields with the advancing hydride interface; however further analysis is required to verify or refute this hypothesis.

4.1.4. References

1. T. Miyashita et al., "*Corrosion and hydrogen pick-up behavior of Zircaloy component of BWR high burnup 9 x 9 Lead Use Assemblies,"* IAEA Technical Meeting on High Burnup Fuel Experience and Economics, Sofia, Bulgaria, 2006.
2. SRIM: http://srim.org/

4.2. Microtensile Testing of Ion-Irradiated Material

One of the challenges for validating predictive simulations is obtaining comparable experimental data. To address the case of predicting mechanical property changes as a function of irradiation damage (as discussed in Section 4.3), we present here a technique for microtensile testing of ion-irradiated material. Complete results are being prepared for publication: B. G. Clark, B. L. Boyce, B. L. Doyle, E. Stech, D. Robertson, R. Dingreville, S. Rajasekhara, T. Buchheit, L. N. Brewer, and K. Hattar, "*Efficient Evaluation of Structural Nuclear Materials: Small-Scale Mechanical Testing of Ion Damaged Materials*," in preparation for ASTM International Selected Technical Papers; B. G. Clark, R. Dingreville, B. L. Boyce, K. Hattar, S. Rajasekhara, B. L. Doyle, D. Robertson, and E. Stech, "*Deformation Behavior of Ion Irradiated Zr-4 Cladding Material: Comparison of Experiments to Modeling*," in preparation for Acta Materialia.

4.2.1. Introduction & Approach

In order to predict the performance of structural materials for extension of current reactor liftetimes and development of next generation reactors, fundamental understanding of changes in material behavior in extreme environments is needed. When considering the effect of irradiation damage due to neutron exposure, one of the challenges is creating displacement damage within a reasonable time frame. Experiments using test reactors can be time consuming due both to lead times for insertion of samples and to the kinetics of neutron-induced damage. To address this, many studies have used ion beam irradiation or implantation to achieve damage on the order of displacements per atom (dpas) or even 100s of dpas within days. Although damage using ion irradiation and implantation is limited to depths on the order of microns, advances in small-scale sample preparation and mechanical testing techniques are enabling an exciting new realm in which ion damaged materials, with nearly uniform damage profiles, can be *quantitatively* assessed for changes in mechanical properties as a function of displacement damage.

Here, experimental data for irradiated Zr-4 cladding material was obtained by producing microtensile specimens (~40 μm thickness, see Figure X) from Zr-4 cladding tubing and irradiating with 26 MeV $^{7}Li^{3+}$ ions to 0.01 and 0.1 dpa. Tensile bars were prepared from Zr-4 cladding tubes as follows: 10 mm x 4 mm rectangles were cut from tub side walls using a diamond saw, and mechanically polished to 80 um in thickness overall. Afterwards, ovals were punched on each side of the rectangle to produce a dog-bone shape, then the gage section was thinned to 40 um in thickness via electropolishing. Ion irradiations were performed by Dr. Ed Stech at the University of Notre Dame. The 26 MeV $^{7}Li^{3+}$ ions were chosen to simulate neutron damage due to their ability to penetrate through the full sample thickness, thus minimizing ion

implantation effects. Following irradiation to desired damage levels, mechanical testing was performed by B. Salzbrenner and B. L. Boyce at Sandia.

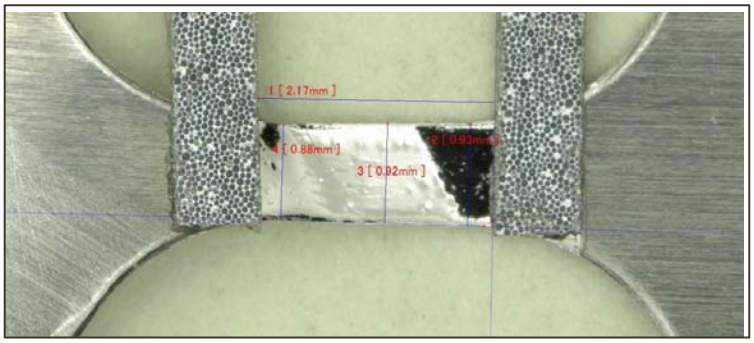

Figure 10. Representative Zr-4 microtensile sample. Gage sections were approximately 1mm in thickness and 2 mm in length.

4.2.2. Results Summary

Testing results show an anticipated increase in stiffness and decrease in ductility with increasing irradiation damage level; see Figure 11. This behavior is consistent with reported literature data for neutron irradiation effects on mechanical properties in metals, e.g. [1].

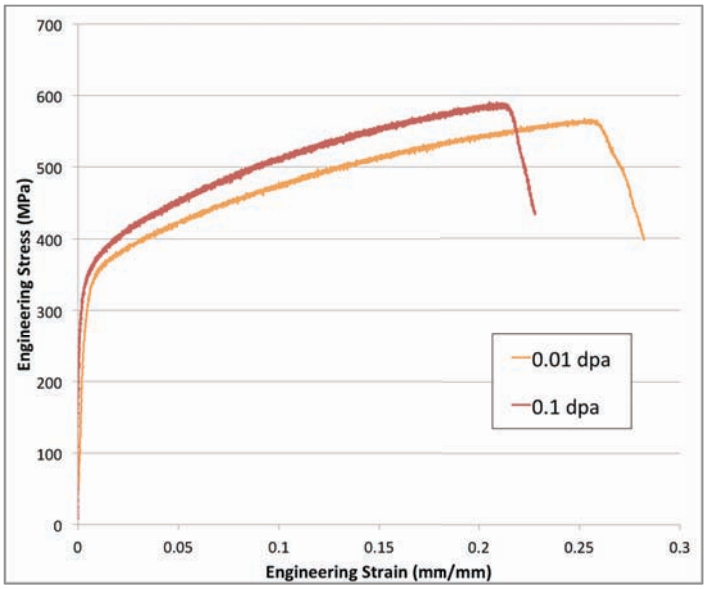

Figure 11. Engineering stress-strain curves for Zr-4 microtensile samples ion irradiated to 0.01 and 0.1 dpa. Higher damage results in an increased yield point, and decreased elongation to failure.

Efforts to incorporate these results for comparison with the simulation method discussed in Section 4.3 are underway. A 3D microstructure will be generated taking into account the initial texture data and irradiated effect distributions to predict mechanical behavior of irradiated Zr-4 for comparison with obtained experimental results.

4.2.3. Conclusions

We successfully demonstrated a technique for preparing small-scale tensile samples from Zr-4 cladding tubing, ion irradiating through the full sample thickness to approximate neutron irradiation damage, and pulling to failure to obtain mechanical property data as a function of irradiation dose. Results showed that 0.1 dpa samples exhibited a higher yield point and reduced ductility compared to 0.01 dpa samples, as anticipated based on reported literature data. These results will be compared to simulated data for irradiated Zr-4 generated using the model discussed below in Section 4.3.

4.2.4. References

1. Singh, B. N., Horsewell, A., Toft, P., Edwards, D. J., 1995. Temperature and dose dependencies of microstructure and hardness of neutron irradiated OFHC copper. Journal of Nuclear Materials 224 (2), 131–140.

4.3. Predictive Simulation for Irradiation Damage Effect on Mechanical Properties

This section highlights results related to development of a predictive simulation for the effect of accumulated irradiation damage on resulting mechanical properties. Although the intent is to extend the model to Zr systems, the present results are for simulation of polycrystalline Cu. Complete results are being prepared for publication: R. Dingreville, "*Stochastic modeling of irradiation hardening of polycrystalline materials*," in preparation for Phil. Mag.

4.3.1. Introduction & Approach

The mechanical behavior of polycrystalline materials subjected to increasing irradiation dose is typically characterized by an increase of the yield strength, a decrease of the ductility and a decrease of work hardening rate [1-4]. These significant alterations in the mechanical properties of an irradiated material are correlated with microstructural changes ranging from crystalline-to-amorphous transitions to the generation of large concentration of point defects and depend upon the crystallographic structure of the materials [5-12]. Irradiation induced degradation of mechanical performances such as the loss of ductility or plastic instability are matters of serious concern from the point of view of structural integrity and lifetime performance of materials used in the structural components of fission or fusion reactors.

Here, a simple but fundamental stochastic crystal plasticity mesoscale model is used to simulate the mechanical response dependence on the irradiation dose of irradiated polycrystals and investigate the possible impact of microstructural attributes on radiation hardening. Defects found in these irradiated materials are treated stochastically. Based on experimental observations, the choice of defects generated (dislocation loops and/or stacking fault tetrahedra), and their associated size and strength are determined randomly and vary with the irradiation dose. The computational model explicitly addresses the effects of microstructure by including realistic topological information: grain morphology, topology, crystallography and irradiation defects. The physics of deformation of fcc microstructures are incorporated through a crystal

plasticity formulation that considers the different slip systems, the elasto-plastic crystallographic anisotropies and the interaction between radiation induced defects and pre-existing defects at the grain level. A set of computer-generated, representative microstructures is used to compare the dose dependence of the yield stress given by this probabilistic model to the uncertainty measurements from experimental data.

4.3.2. Results Summary

Due to readily available experimental data for comparison, the stochastic irradiation hardening model was implemented into Sandia's time-explicit parallelized Material Point Method (MPM) paradigm [13-14] and applied to model irradiation hardening in both copper single crystals and polycrystals. The elastic constants and hardening parameters (materials properties for unirradiated materials) introduced in the constitutive model were calibrated using a representative three-dimensional (3D) microstructure containing 350 grains and based the experimental results of Singh et al. [1]. The irradiation damage-dependent material constants were approximated from various experimental observations of irradiation-induced defects and from the initial yield strength of the irradiated stress-strain response.

The predicted uniaxial stress-strain curve for a polycrystalline material is plotted in Figure 12. The general behavior of the constitutive model shows that as the dose increases the initial yield point increases. Figure 4 shows the dose dependencies of increase in yield stress vs. dpa, presented in the log–log format to reveal two distinct regimes: the low-dose and the high-dose regimes. The trend can be explain by the fact that the defect-cluster density is initially linearly proportional to fluence at low doses (~0.0001 dpa) and exhibited a square-root dependence before saturation.

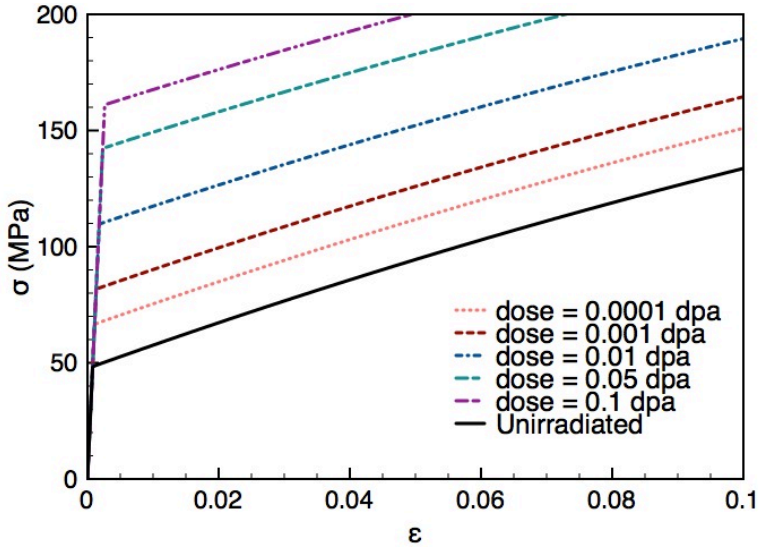

Figure 12. Simulated effective stress-effective strain behavior of an irradiated OFHC copper polycrystal with varying doses of irradiation.

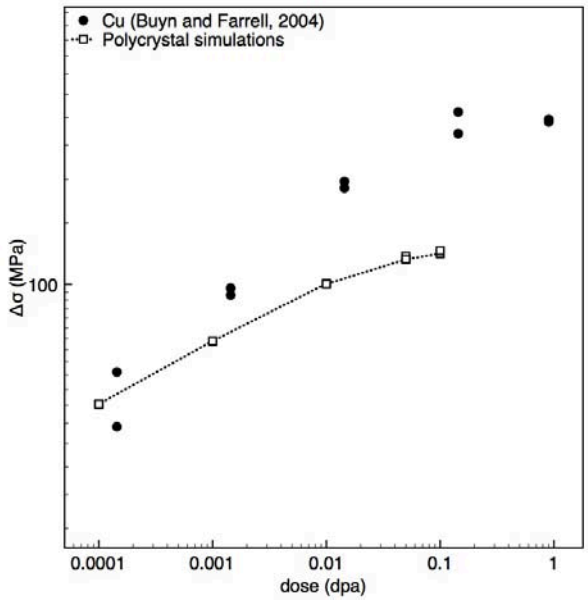

Figure 13. Dose dependence of the yield stress change due to irradiation for copper single crystals. Results predicted by the stochastic radiation hardening model are compared to experimental results from [15].

4.3.3. Conclusions

The mesoscale stochastic hardening model presented was developed with information about irradiation induced defects passed by statistics from experimental results about these defects. The objective of such model was to capture the dominant physical mechanisms and their disparity as observed experimentally. In principle, this constitutive model can be combined with a model for radiation defect evolution (defect type, size and number density) as a function of irradiation and material variables to obtain a truly predictive model for the mechanical behavior changes of irradiated materials. Further, this constitutive model framework is general and can be applied to both more complicated fcc metals and alloys, such as austenitic stainless steels, as well as hcp alloys. The implementation of a hcp model will be the focus of future modeling efforts and will require a temperature dependent dislocation velocity law to account for the inherent lattice resistance and the materials response to strain localization and the formation of adiabatic shear bands. Such a modeling effort can be used as a tool to evaluate and rank the importance of radiation-induced effects on irradiated materials.

4.3.4. References

1. Singh, B. N., Horsewell, A., Toft, P., Edwards, D. J., 1995. Temperature and dose dependencies of microstructure and hardness of neutron irradiated OFHC copper. Journal of Nuclear Materials 224 (2), 131–140.
2. Pawel, J. E., Rowcliffe, A. F., Lucas, G. E., Zinkle, S. J., 1996. Irradiation performance of stainless steels for ITER application. Journal of Nuclear Materials 239, 126–131.
3. Farrell, K., Byun, T. S., 2003. Tensile properties of ferritic/martensitic steels irradiated in HFIR, and comparison with spallation irradiation data. Journal of Nuclear Materials 318, 274–282.

4. Fabritsiev, S. A., Pokrovsky, A. S., 2007. Effect of irradiation temperature on microstructure, radiation hardening and embrittlement of pure copper and copper-based alloy. Journal of Nuclear Materials 367–370, Part B, 977–983.
5. Seeger, A. K., 1958. Deformation of neutron-irradiated copper single crystals. In: 2nd UN International Conference on Peaceful Uses of Atomic Energy. Vol. 6. United Nations, New York, p. 250.
6. Blewitt, T. H., Coltman, R. R., Jamison, R. E., Redman, J. K., 1960. Radiation hardening of copper single crystals. Journal of Nuclear Materials 2 (4), 277–298.
7. Eyre, B. L., 1973. Transmission electron microscope studies of point defect clusters in fcc and bcc metals. Journal of Physics F: Metal Physics 3 (2), 422–470.
8. Sharp, J. V., 1974. Deformation of neutron irradiated copper alloys. Acta Metallurgica 22 (4), 449–457.
9. English, C. A., Eyre, B. L., Muncie, J. W., 1987. Low-dose neutron irradiation damage in copper. Philosophical Magazine A 56 (4), 453–484.
10. Dai, Y., Gavillet, D., Paschoud, F., Victoria, M., 1994. Mechanical properties and microstructure of 600 MeV proton irradiated copper single crystals. Journal of Nuclear Materials 212–215, Part A, 393–398.
11. Weber, W. J., 2000. Models and mechanisms of irradiation-induced amorphization in ceramics. Nuclear Instruments and Methods in Physics Research Section B: Beam Interactions with Materials and Atoms 166–167, 98–106.
12. Zinkle, S. J., Matsukawa, Y., 2004. Observation and analysis of defect cluster production and interactions with dislocations. Journal of Nuclear Materials 329–333, Part A, 88–96.
13. Zhang, L., Dingreville, R., Bartel, T. J., Lusk, M. T., 2011. A stochastic approach to capture crystal plasticity. International Journal of Plasticity 27 (9), 1432–1444.
14. Bartel, T. J., Dingreville, R., Robbins, J., Lusk, M. T., Zhang, L., Brewer, L. N., 2012. iMPALE - Ma- terial Point Arbitrary Lagrangian Eulerian code: A time implicit/explicit integration 3-D lagrangian material point method code. Sandia Technical Report SAND2012-0957, Sandia National Laboratories, Albuquerque, NM.
15. Buyn, T. S., Farrell, K., 2004. Irradiation hardening behavior of polycrystalline metals after low temperature irradiation. Journal of Nuclear Materials 326 (2-3), 86–96.

4.4. TEM Analysis of Small Scale Post-Reactor Cladding Samples

To further understand the accumulation of defects and microstructural changes occurring during extended neutron irradiation of cladding, post-reactor Zr-4 samples were prepared at Idaho National Labs and shipped to Sandia National Labs for subsequent TEM analysis. Provided in this section are details of the sample preparation and shipment, along with preliminary TEM images.

4.4.1. Introduction & Approach

As detailed in Section 2, predicting the condition of cladding material after long term dry storage is complicated by lack of understanding of the ‘starting’ microstructure after in-reactor use. This is in part due to difficulties in obtaining and preparing such material for microstructural analysis: After use in a reactor, cladding material is radioactive, making it difficult to handle, prepare

samples, and transport. Thus specialized facilities are required for such work, such as a hot cell and other equipment approved for use with radioactive material.

To better understand the microstructure of post-reactor cladding, we established a collaboration with Melissa Teague at Idaho National Labs. INL has both inventory of post-reactor material as well as specialized facilities for sample preparation of radioactive material. There, Doug Porter identified legacy material consisting of UO2 fuel rods with Zr-4 cladding that had been used in the Belgian BR3 reactor up to ~ 40 GwD/MTU of burnup. Full details of the fuel rods can be found in INL's 1984 report, titled: "Characteristics of UO2-Zr Fuel Rods Irradiated in the BR3 Reactor." [1]

A portion of the fuel rod was sectioned, defueled, and mounted within INL's Hot Cell facility. After sectioning and defueling, the sample volume was low enough to be acceptable for handling and analysis within INL's Electron Microscopy Laboratory (EML). At the EML, the mounted section of BR3 cladding was loaded into the Hot-FIB for TEM sample preparation. This Hot-FIB is unique as being the only instrument in the country able to examine a full range of radioactive materials from activated metals to irradiated transuranic fuels. The Hot-FIB allows for the fabrication of TEM and micro-mechanical test specimens that are impossible to fabricate using traditional preparation methods.

Six samples were prepared and extracted from the mounted BR3 cladding; the locations are shown in Figure 14. Three samples were taken along the radial direction at the inner, middle, and outer portions of the cladding (Figure 14a), and three analogous samples were taken along the circumferential direction (Figure 14b). Samples were extracted via OmniProbe needle and affixed to the posts of an Omniprobe lift-out TEM grid via Pt deposition. Because of the extremely small size of samples prepared using the FIB (FIB TEM samples are ~3 million times smaller than a traditional TEM disk), the resulting samples had radioactivity below detection levels, allowing for safer handling of samples and utilization of other advanced equipment without significant contamination or exposure concerns.

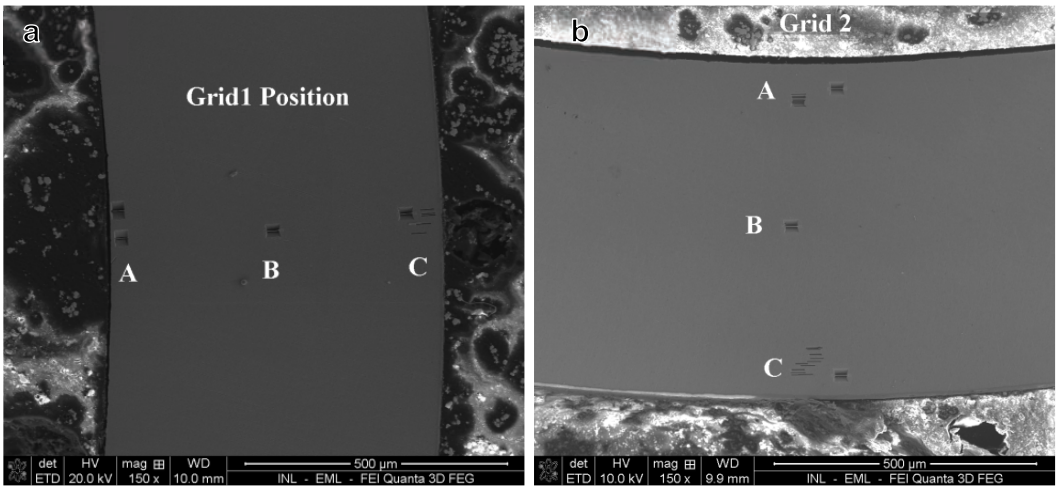

Figure 14. Location of FIB-prepared cross-sectional TEM samples from Zr-4 cladding irradiated to 40 GwD/MTU in the Belgian BR3 reactor. Samples were extracted at the inner, middle, and outer portions of the cladding and oriented (a) radially and (b) circumferentially.

The FIB-extracted and mounted samples were left in the FIB sample mount, where they were secured between two plates connected by a pressure screw, and then placed in a South Bay Sample Saver fitted with shelves. The Sample Saver was then pulled to vacuum and sealed before shipment to Sandia National Labs.

4.4.2. Results Summary

Prior to shipment, a representative sample was imaged in INL's JEOL 2010 TEM operated at 200 keV to check for electron transparency, see Figure 15. The process of sample preparation and mounting was demonstrated successful, and Figure 15c shows that the sample was electron transparent and ready for further TEM analysis. The post-reactor Zr-4 cladding was full of irradiated defects, residual stress (manifested as sample bending), and precipitates.

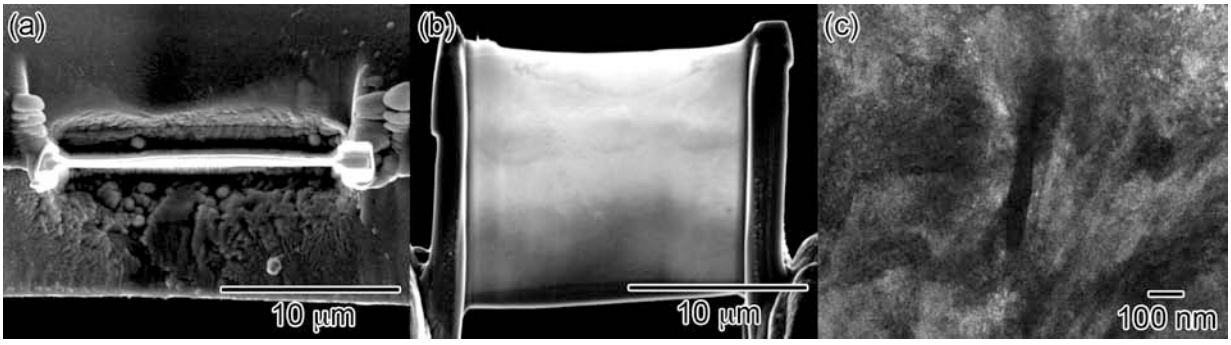

Figure 15. FIB-milled TEM sample prepared at INL of Zr-4 cladding following irradiation in the Belgian BR3 reactor. (a) Top-down view following FIB milling, (b) Side view of sample after mounting onto Omniprobe liftout grid, and (c) TEM image taken near top surface of the sample, verifying electron transparency. Irradiation damage and residual stress is visible throughout; the center of the image shows a 200 nm precipitate.

Following preparation of all six samples, as described in Figure 14, samples were shipped to Sandia for further analysis. Once received, there was some delay prior to analysis due to the need to set up a procedure for handling the Zr-4 samples while minimizing the opportunity for oxidation. Following the successful development of a dry nitrogen glove bag procedure for extracting samples from the Sample Saver and inserting them in the TEM, samples were imaged using Sandia's Tecnai ChemiSTEM operated at 200 keV.

Unfortunately, upon opening the Sample Saver container within the glove bag, it was clear that the samples were not securely affixed to the shelves and had come loose in shipment. The shelves had o-rings through with the stub of each FIB mount was inserted, however this pressure seal was not sufficiently secure. This resulted in extensive damage to the samples such that no further analysis could be performed; see Figure 16.

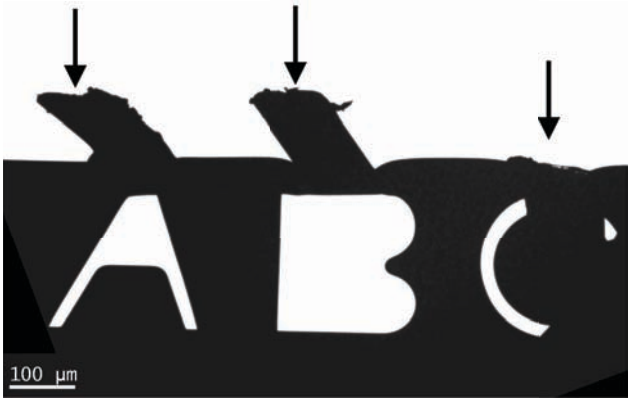

Figure 16. TEM image of as-received, post-reactor Zr-4 samples prepared at and shipped from INL. Samples were affixed to the posts above the letters A, B, and C (arrowed), but these posts were badly bent after the FIB mount came loose in shipment, resulting in damage to the Zr-4 samples and precluding any further TEM analysis.

4.4.3. Conclusions

A procedure for preparation of small-scale samples at INL with subsequent shipment to SNL for further analysis was successfully demonstrated. However, there were some lessons learned during this process:

- For shipment purposes, it is critical that the shelves be those designed for FIB sample mounts, e.g. [2], so that there is a screw for tightening the mount post to the shelf. Otherwise, it is easy for the samples to come loose in shipment resulting in damage.
- Samples should be analyzed as quickly as possible to avoid any potential issues with sample oxidation. The seal of the Sample Saver is not stable indefinitely.
- For Zr-based samples, a glove bag procedure with dry nitrogen should be used to minimize air exposure in transferring the samples from the Sample Saver to the TEM or other instrument for analysis.

4.4.4. References

1. J. A. Adams and B. R. Dabell, "Characteristics of UO2-Zr Fuel Rods Irradiated in the BR3 Reactor," Idaho National Laboratory Report, FIN No. A6305, November 1984.
2. http://www.southbaytech.com/diva/divaPOP/divaPOPgold_img.htm?i=http%3A%2F%2Fwww.southbaytech.com%2Fshop%2Fshopimages%2FSS100-FIB.jpg&c=&a=SS100-FIB&h=1&n=1&x=&s=15&t=

5. CONCLUSIONS

Through this LDRD, we made significant contributions to the understanding of microstructural degradation mechanisms in Zr-based claddings towards development of high fidelity predictive simulations for long term dry storage of used nuclear fuel assemblies. Experiments and modeling efforts were focused on two key aspects related to mechanical property changes: hydride formation and accumulation of irradiation defects.

Key results and conclusions were as follows:

- Formation of hydride was found to be influenced by Zr-alloy composition. Zr-2 and Zr-4 alloys formed hydride at an order of magnitude faster rate than Zirlo™. This was verified through ERD, cross-section TEM imaging, and electrochemical experiments. The higher percentage of Nb in the Zirlo™ samples is believed to alter the surface potentials such that hydrogen uptake is hindered.
- Hydride formation was also shown to be influenced by the number, size, and distribution of irradiated defects in Zr-4. Low, 1.5 dpa samples with 100 nm interstitial loops densely distributed throughout the sample significantly hindered hydride formation, whereas high, 38 dpa samples with 150-200 nm interstitial loops distributed sparsely throughout the sample saw hydride formation comparable to that of unirradiated samples. This observation is believed to be the result of a fairly uniform strain field produced when loops are closely spaced that interacts with and hinders the progression of the hydride front.
- A microtensile test method was developed for studying the effect of ion irradiation on mechanical properties of Zr-4 was presented. Results showed an increase in the yield point and decrease in the elongation to failure with increasing dpa. Data obtained will be compared to the results of a stochastic model for simulating the effect of irradiated defects on mechanical properties, also developed in this LDRD.
- For the first time, formation of hydride in Zr-4 was observed *in situ* using an environmental heating stage. This could impact future studies of hydride formation, including studies of hydride reorientation.
- A method for preparation of radioactive, post-reactor nuclear cladding at INL and subsequent shipment to Sandia was developed and demonstrated. This result highlights opportunities for continued collaboration and cooperation with INL, taking advantage of legacy materials and facilities for handling hot materials there and the advanced TEM and microscale mechanical testing facilities and expertise here.

APPENDIX A: USE OF ION BEAMS

As stated above, ion beams from the Ion Beam Lab – IBL - Tandem Van de Graaff were used in this research to both simulate the displacement damage produced by fission neutrons and to measure the concentration depth profile of H after the Zircaloys were charged. This appendix provides the details of both these ion beam applications.

A1. Ion-Neutron SIMulation - INSIM

To explore the impact that fission neutron induced displacement damage has on the hydrogen uptake characteristics, the Zircaloy samples were ion irradiated with 25 MeV Au ions to produce 0.1, 1 and 25 dpa levels of damage, after which they were charged with hydrogen and examined with Elastic Recoil Detection – ERD - that is described in the next section. The use of ions to simulate neutron damage is called INSIM in the IBL, and this was employed because it is easy to control, results in no sample activation, and can quickly induce damage that is equivalent to long term neutron radiation, which cladding materials experience during service.

There is no direct way to measure the dpa level produced either by neutrons or ions, and therefore one must rely on theoretical calculations. To validate this approach, two calculations were used and compared for the dpa's produced by the 25 MeV Au ions in pure Zr.

The first was the Robinson model [1,2] which is analytical and was developed in the 1960s. The results are shown in Figure A17 below.

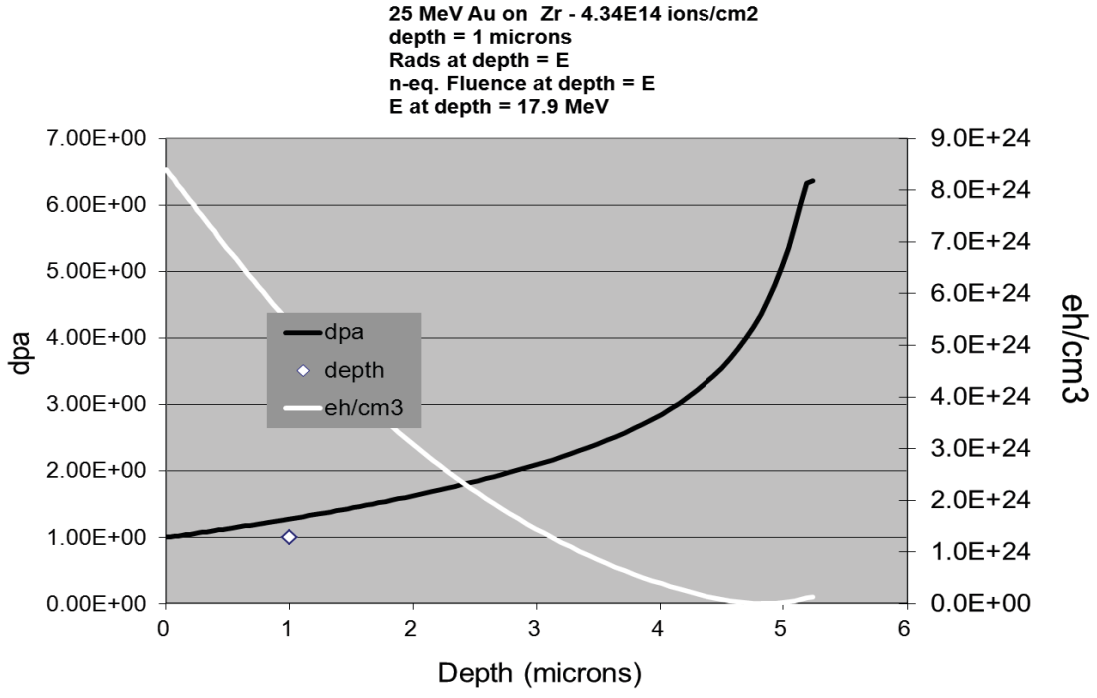

Figure A17. Robinson model calculation of dpa vs. depth for 25 MeV Au on Zr. The results of this calculation indicate that a fluence of 4.3e14 Au ions/cm2 will produce atomic displacements at a level of 1 dpa at the surface of the Zr.

The second approach was to use Ziegler's SRIM code [3] which is easily downloaded from the internet. Using SRIM the fluence required for 25 MeV Au to produce 1 dpa is a little less, 3.9e14. The following figure shows the distribution of collision events and ion ranges calculated using SRIM, and the table compares the dpa levels calculated for some of the actual exposures made in the IBL for Zr-2, Zr-4 and Zirlo samples. The table is divided into two parts because the beam spot area was reduced for the ~25 dpa damage level to reduce the time required for exposure, see Figure A18.

	x	y	A					
area	0.2	0.2	0.04	cm2				
					robinson		SRIM	Au conc in
					dpa	actual au/cm2	dpa	first micron
1	zr2-1	100000	2.5	3.90625E+14	0.90	3.90625E+14	1.00	9.07978E-07
2	zr4-1	100000	2.5	3.90625E+14	0.90	3.90625E+14	1.00	9.07978E-07
3	ziro-1	100000	2.5	3.90625E+14	0.90	3.90625E+14	1.00	9.07978E-07
4	zr2-2	10000	0.25	3.90625E+13	0.09	3.90625E+13	0.10	9.07978E-08
5	zirlo-2	10000	0.25	3.90625E+13	0.09	3.90625E+13	0.10	9.07978E-08
	x	y	A					
area	0.08	0.2	0.016	cm2				
					robinson		SRIM	
runs	sample	bcis	puC	au/cm2	dpa	actual au/cm2	dpa	
7	zr2-3	1000000	25	3.90625E+15	22.49	9.76563E+15	25.0	2.26994E-05
8	zr4-3	1000000	25	3.90625E+15	22.49	9.76563E+15	25.0	2.26994E-05
	zirlo-3	1000000	25	3.90625E+15	22.49	9.76563E+15	25.0	2.26994E-05

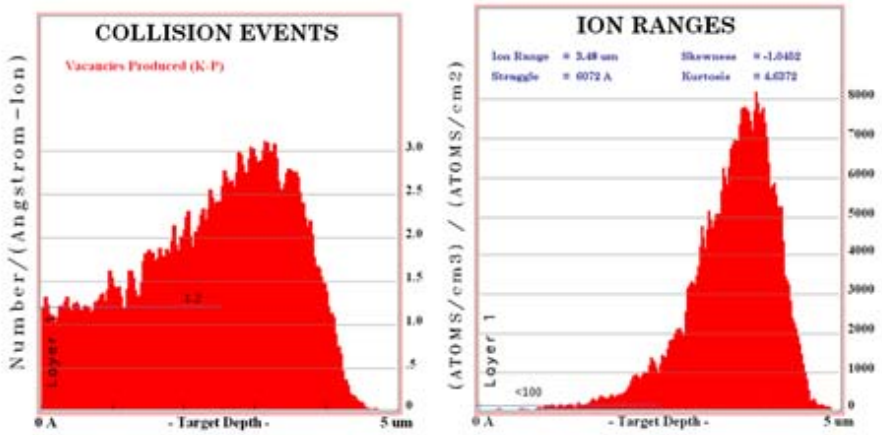

Figure A18. SRIM calculations of the number of vacancies caused by the collision event and ion range distribution for 25 MeV Au on Zr. The table shows data from actual exposures to Zr-2, Zr-4 and Zirlo to levels of 0.1, 1 and 25 dpa.

The regions on the zircaloy samples that were exposed to the Au beam could be seen optically as shown in Figure A19. These regions were marked by punching small indentations into the sample at the edge of each region. This was done because these regions were not so visible after H charging, and the fiducial marks were quite useful for defining the region to analyze using ERD and to produce the cross sectioned samples using the FIB.

Figure A19. Optical microscope image of Zr-4 sample exposed to 25 MeV Au ions to a damage level of 25 dpa. The region exposed is the dark rectangle between the two fiducial marks.

A2. Elastic Recoil Detection – ERD

The IBL at Sandia has a long history in the development of ERD [4-10] going back to the 1970s, and even pioneered the technique using MeV He beams. He-ERD depth profiling of H isotopes is now just about as common as Rutherford Backscattering Spectrometry – RBS, and has been used by 100s of scientists around the world.

Hydrogen uptake in the Zircaloy samples was examined with ERD using the IBL Tandem Van de Graaff accelerator with 10 MeV He^{2+} and 34 MeV Si^{5+} ions. A schematic of the experiment and some sample data is shown in Figure A20.

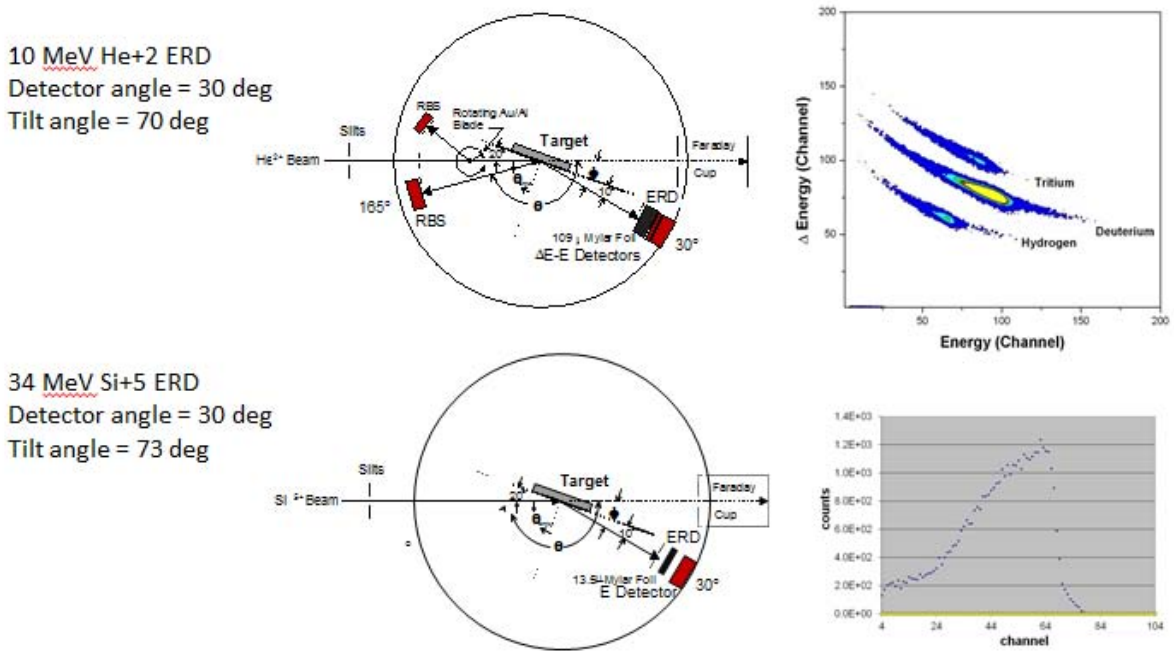

Figure A20. Schematic of beam-target-detector geometries for He-ERD and Si-ERD together with representative spectra. The 10 MeV He-ERD system uses a dE-E particle telescope for the detection of the recoiled H-isotopes after passage through a 109 micron Mylar range foil, and in the case of this research, only the hydrogen, or protium, peak would be present in the counts vs. dE and E spectrum. For the 34 MeV Si-ERD, just a standard E surface barrier detector is used to detect the recoiled H after passage through a 13.5 micron Mylar range foil.

A2.1. He-ERD

The obtained raw yield data, in the form of yield versus channel number, was analyzed using a spectral scaling approach developed by Brice and Doyle [10]. In this approach, the raw yield data is scaled to appear as if the recoil cross section ($d\sigma/d\Omega$) and stopping power ($dE_{detected}/dx$) as a function of depth are constant and equal to that at the surface. The H recoil cross sections by He were taken from the extrapolated calculations of Gurbich on the IBANDL website [11], and parametrically represented by the equation:

$$\sigma = c + ae^{E/b} + de^{-\left[\frac{(E-f)^2}{g^2}\right]}$$

Where σ is in mbarns/steradian, E is the He Energy in MeV, and
a=4700
b=0.5
c=270
d=500
f=8.8
g=3
The Gurbich cross sections together with the fit to the equation above is shown in Figure A21.

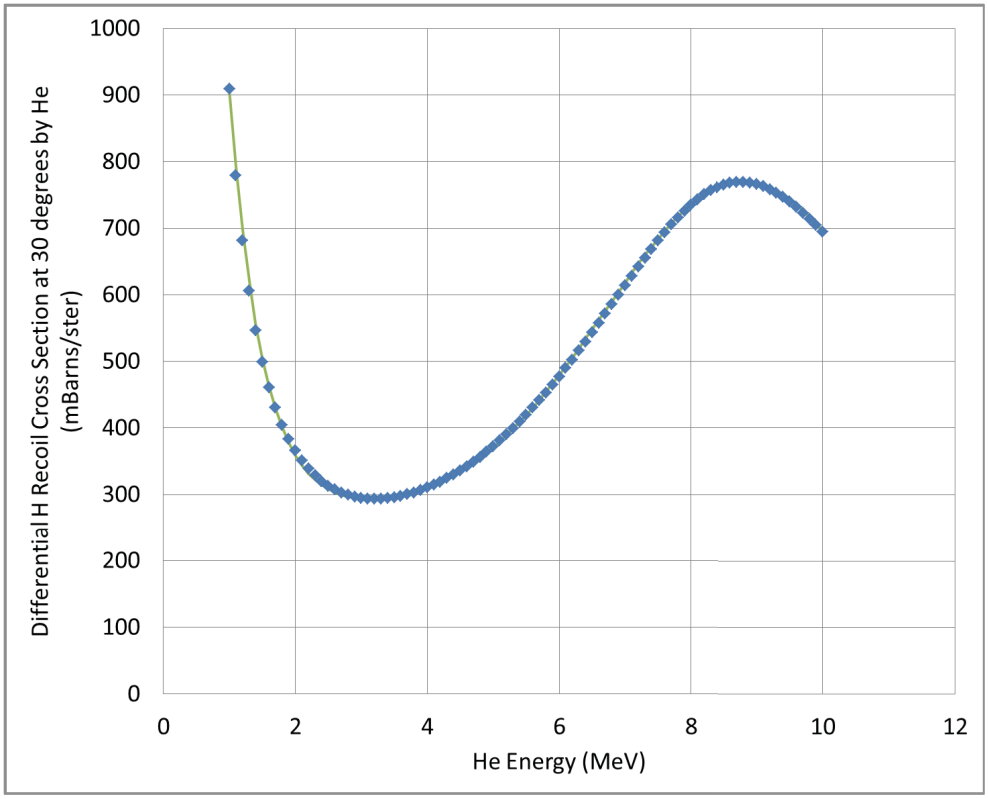

Figure A21. Parametric representation of the He ERD recoil cross section of H at 30 degrees. This fitted representation was used in the spectral scaling program to convert the He-ERD raw data into quantitative H concentration depth profiles in the Zircaloys.

The H recoil cross sections for the Si ions were Rutherford.

$$\sigma_{Rutherford} = \left[\frac{Z_p Z_l (M_p + M_l)}{M_l E}\right]^2 \frac{1}{\sin^4 \theta}$$

Where Z_p=14, Z_l=1, M_p=28, M_l=1, θ=30°, and E is the energy of Si as it passes thru the sample.

The scaled yield data was input in the yield equation given by $C_H = \dfrac{Y_r(E_d)\cos\theta \, dE_d/dx}{Q\, d\sigma_r(E_o', \phi)/d\Omega\, \Omega\, \delta E_d}$, where C_H is the hydrogen concentration, Y_γ the yield, E_d the energy of the recoiled atoms at the detector, cos θ the tilt angle of the sample (73°), dE_d/dx the stopping power, Q the number of ions, $d\sigma_r(E_o', \phi)/d\Omega$ the differential cross-section, Ω the detector solid angle, and δE_d the channel width. This equation was solved for hydrogen concentration, the channel number was converted to depth, and the result re-plotted as concentration (C_H) vs. depth to obtain H-concentration profiles as a function of charging duration as shown in Figure A22.

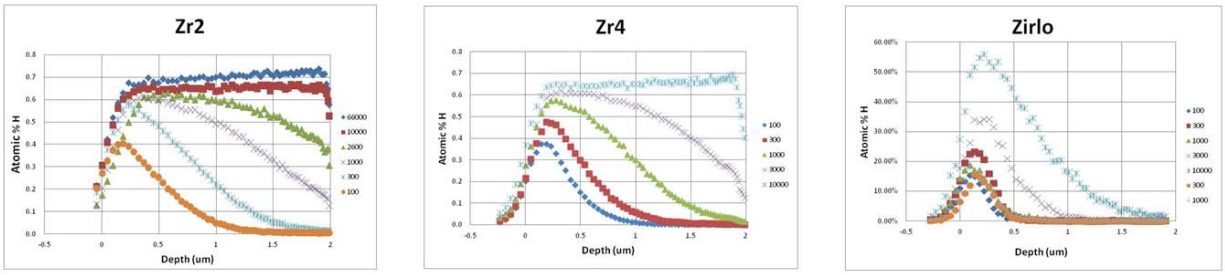

Figure A22. Spectrally scaled H profiles in Zr-2, Zr-4 and Zirlo using 10 MeV He-ERD. The exposure time of each electrolytic charging is given in the legend.

Areal densities in H atoms/cm2 , were then determined by integrating these profiles, and then converted to equivalent ZrH_2 thicknesses - d_{eq} - by dividing these areal densities by the concentration of H atoms in ZrH_2 – 7.23e22 H/cm^3. d_{eq} is plotted as a function of time on a log-log scale in order to determine hydrogen ingress kinetics in Figure A23.

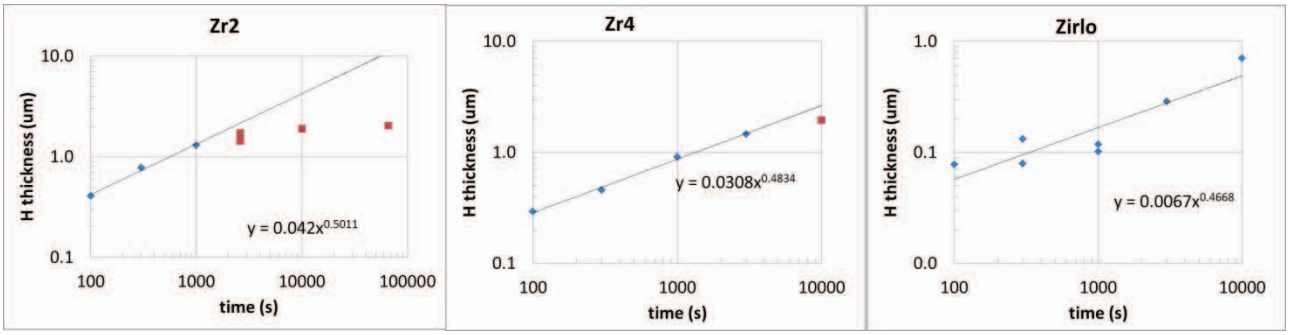

Figure A23. Log-Log plot of the equivalent ZrH_2 thicknesses in Zr-2, Zr-4 and Zirlo as a function of electrolytic charging time. The straight line fits together with their parameters are also shown.

The straight lines fit the data fairly well for but only for thicknesses ~< 2 microns. This is because the He-ERD technique can only measure the profile in the top ~2 microns of the zircaloy samples, and so the equivalent thickness saturates at ~2 microns using the integrated areal densities. The powerlaw fits to the data has an exponent of ~ 0.5 which indicates the diffusion of H in the growing hydride layer controls the kinetics of this H loading process. The diffusion equation that controls the growth of the hydride is therefore:

$$d_{eq} = (Dt)^{1/2}$$

where D is the diffusion coefficient and t is the time. To determine these diffusion coefficients, the equivalent thicknesses are plotted as a function of time$^{1/2}$ where the slope of the straight line fits provide D$^{1/2}$. This data and fits are plotted in Figure A24.

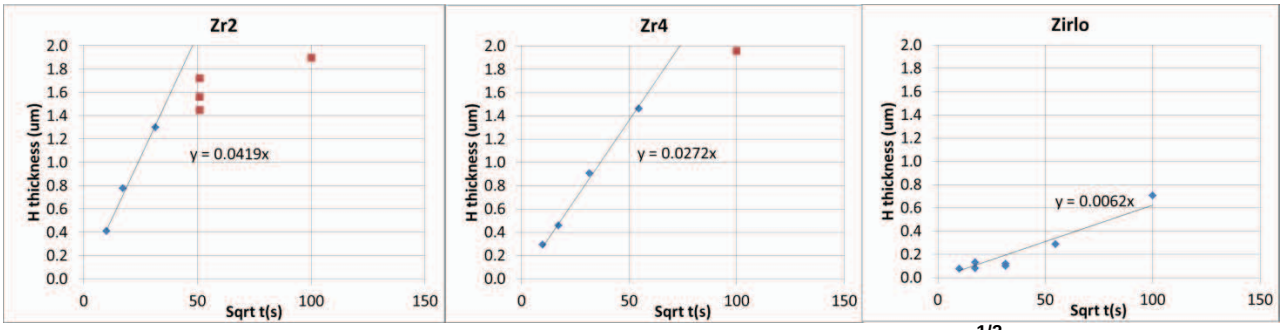

Figure A24. Plot of the equivalent hydride thickness as a function of $t^{1/2}$. The straight line fits are also plotted together with their fitting parameters.

Based on this ERD analysis, we find that $D_{Zr\text{-}2} \sim 1.7 \times 10^{-11}$ cm^2/s, $D_{Zr\text{-}4} \sim 7.4 \times 10^{-12}$ cm^2/s, and $D_{Zirlo} \sim 3.8 \times 10^{-13}$ cm^2/s. See the main part of this LDRD Report for further discussion of these measurements and their comparison to the TEM measurements of H incursion.

A2.2. Si-ERD

The Si-ERD was used on samples damaged with the Au beam. This type of ERD had the advantage compared to the He-ERD of being able to focus the 34 MeV Si beam into a spot smaller than the Au irradiation area, which of course was a requirement of the measurement. It had a disadvantage because its analysis depth range was only a little over 1 micron. This limited the electrolytic charging times to be less than 1000s, and even then some of the profiles obviously extended beyond the range of the analysis. The results of the Si-ERD effective hydride thicknesses should therefore be considered as lower limits, especially for the 1000s exposures.

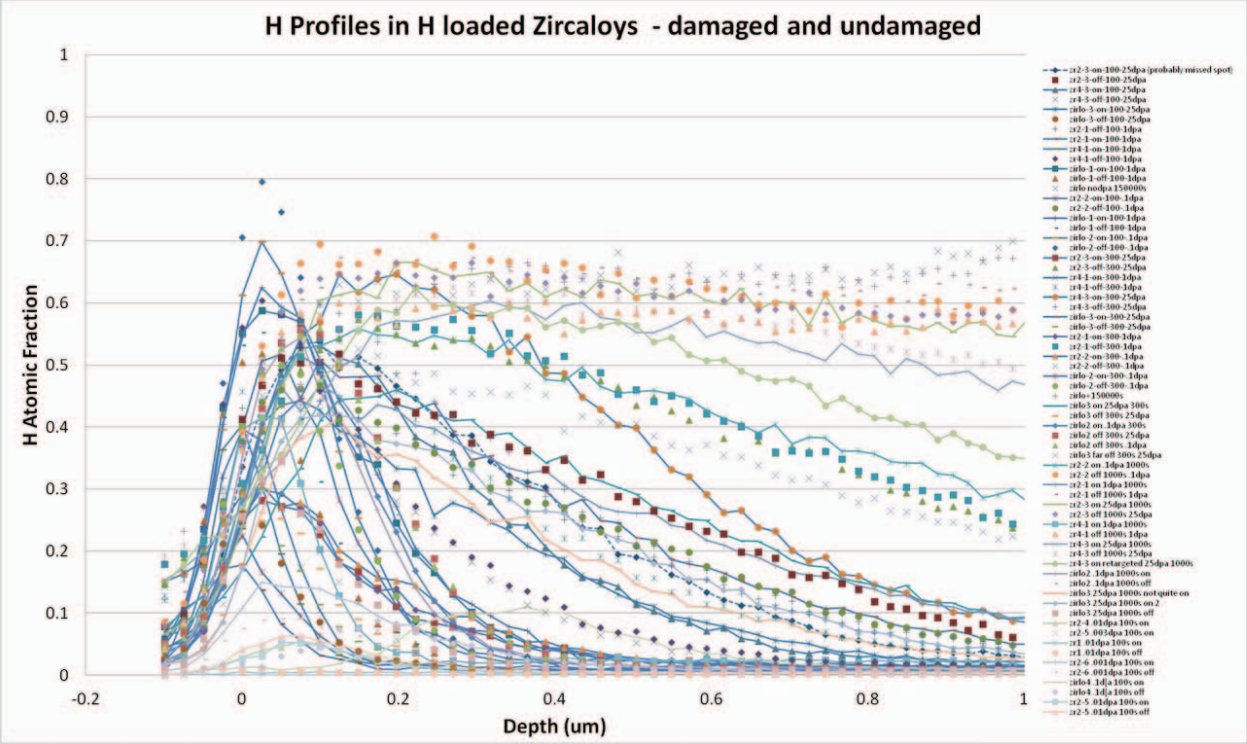

Figure A25. H profiles of electrolitically exposed Zr-2, Zr-4 and Zirlo samples for 100, 300 and 1000 seconds at 25 MeV Au predamaged levels of 0, 0.1, 1.0 and 25 dpa.

Figure A25 above shows all the H profiles measured on the electrolitically exposed Zr-2, Zr-4 and Zirlo samples for 100, 300 and 1000 seconds at 25 MeV Au predamaged levels of 0, 0.1, 1.0 and 25 dpa. As with the He-ERD these profiles resulted by using the spectral scaling algorithm. The data points that are connected by lines are for the samples that have sustained damage, and those without line connections are in regions away from the damage spot.

As with the He-ERD, these profiles were integrated to get areal densities, and the areal densities converted into equivalent hydride thicknesses. The undamaged Si-ERD results are plotted together with the He-ERD results for Zr-2 in Figure A26. In Figure A26, we plot all of the analyses of the profiles displayed in Figure A25.

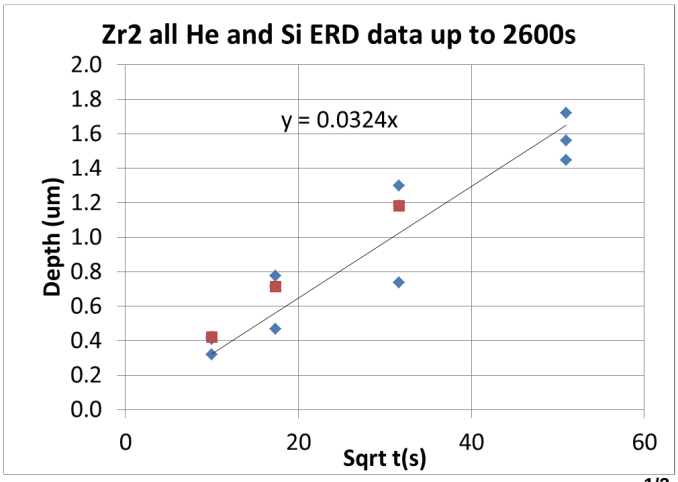

Figure A26. Equivalent hydride thickness vs. $t^{1/2}$ for undamaged Zr2 analyzed using He-ERD (blue diamonds) and Si-ERD (red squares). The two techniques agree within errors for the Zr-2 and Zr-4 and Zirlo (not shown).

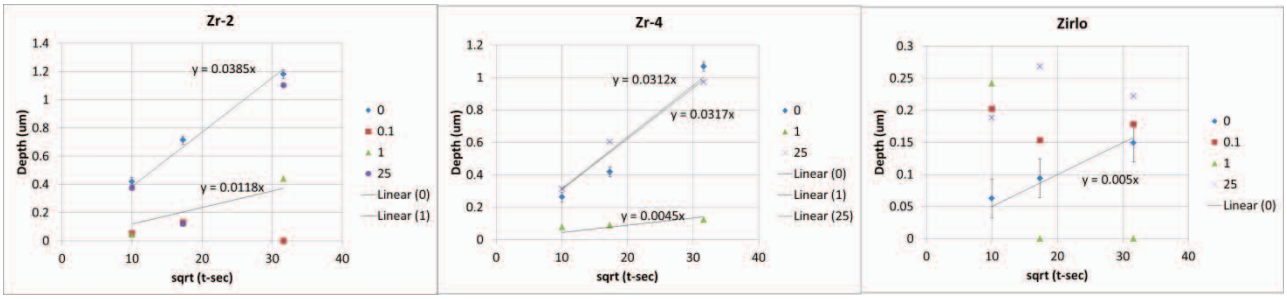

Figure A27. Equivalent hydride thickness measured using Si-ERD for electrolitically exposed Zr-2, Zr-4 and Zirlo samples for 100, 300 and 1000 seconds at 25 MeV Au predamaged levels of 0, 0.1, 1.0 and 25 dpa. Linear fits are also indicated, and used to extract diffusion coefficients as before. The legends indicate dpa damage levels.

The data plotted in Figure A27 show that when the Zr-2 and Zr-4 is damaged to 0.1-1.0 dpa, that the H incursion is much reduced, but at 25 dpa, it seems to return to undamaged levels. The results for the Zirlo are considered inconclusive as regards a damage effect, which appears to be quite small and difficult to quantify from this data.

In Figure A28, we plot the H diffusion coefficients for electrolitically exposed Zr-2, Zr-4 and Zirlo samples for 100, 300 and 1000 seconds at 25 MeV Au predamaged levels of 0, 0.1, 1.0 and 25 dpa. Again the results for Zirlo are really inconclusive due to the size of the error bars and the very small effective hydride thicknesses that resulted.

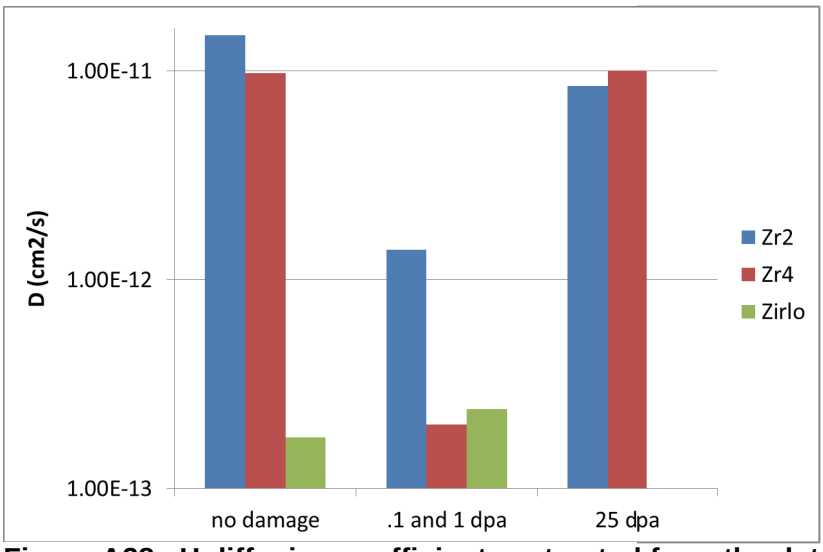

Figure A28. H diffusion coefficients extracted from the data plotted in Figure A27.

A3. Conclusions

Ion beams from the IBL Tandem are quite useful to simulate fission neutron damage in these Zircaloy cladding materials and for the ERD H-profile analysis of electrolytically H-charged Zircaloys. These techniques, partially developed by this LDRD, could be employed for a wide range of materials that are exposed to high energy fission or fusion neutrons. As such, these developments will continue to have great value to future fission and fusion materials research and development that occurs at Sandia, and other US labs engaged in these activities.
Future activities related to this LDRD include:

a. The samples were not actively cooled during Au exposure, and so their temperature was really not known. This could even explain why the 25 dpa results are so similar to the zero damage results, i.e. the damage could have been annealed out by the beam. To ameliorate this, the 25 dpa results should be repeated with active cooling and the surface temperature monitored.
b. Since the effective thickness of the hydrides that formed for the Zirlo cladding was so small for 1000s electrolytic exposures, these exposures should be increased significantly.
c. Because of a difficulty encountered in the precise positioning of the focused Si beam into the Au irradiated spot, a scanning system on the IBA millibeam system should be implemented and then 2d maps of the effective hydride thickness could be made.
d. By using much thicker Mylar range foils, high energy He-ERD could be performed on the IBA millibeam system using the 10 MeV He. Calculations indicate that if a 109 micron Mylar range foil is employed, and the fact that the dE detector is not used in this ERD system, the analysis depths for H could be extended to over 7 microns!

A4. References

1. INFLUENCE OF SCATTERING LAW ON RADIATION DAMAGE DISPLACEMENT CASCADE, ROBINSON MT, PHILOSOPHICAL MAGAZINE Volume: 12 Issue: 118 Pages: 741- , 1965
2. INFLUENCE OF SCATTERING LAW ON RADIATION DAMAGE DISPLACEMENT CASCADE .2, ROBINSON MT, PHILOSOPHICAL MAGAZINE Volume: 17 Issue: 147 Pages: 639-, 1968
3. SRIM: http://srim.org/
4. TECHNIQUE FOR PROFILING H-1 WITH 2.5-MEV VAN DE GRAAFF ACCELERATORS, DOYLE BL; PEERCY PS, APPLIED PHYSICS LETTERS Volume: 34 Issue: 11 Pages: 811-813, 1979
5. HIGH ACCURACY, HIGH ENERGY He-ERD ANALYSIS OF H, D AND T, Browning JF; Langley RA; Doyle BL; et al., NUCLEAR INSTRUMENTS & METHODS IN PHYSICS RESEARCH SECTION B-BEAM INTERACTIONS WITH MATERIALS AND ATOMS Volume: 161 Pages: 211-215, 2000
6. CROSS-SECTIONS FOR THE ELASTIC RECOIL OF HYDROGEN ISOTOPES FOR HIGH ENERGY HELIUM IONS, Browning JF; Banks JC; Wampler WR; et al., NUCLEAR INSTRUMENTS & METHODS IN PHYSICS RESEARCH SECTION B-BEAM INTERACTIONS WITH MATERIALS AND ATOMS Volume: 161, Pages 300-305, 2000
7. TECHNIQUE FOR PRODUCTION OF CALIBRATED METAL HYDRIDE FILMS, Langley RA; Browning JF; Balsley SD; et al., JOURNAL OF VACUUM SCIENCE & TECHNOLOGY A-VACUUM SURFACES AND FILMS Volume: 19 Issue: 5 Pages: 2706-2708, 2001
8. ROUND ROBIN ANALYSES OF HYDROGEN ISOTOPE THIN FILMS STANDARDS, Banks JC; Browning JF; Wampler WR; et al., NUCLEAR INSTRUMENTS & METHODS IN PHYSICS RESEARCH SECTION B-BEAM INTERACTIONS WITH MATERIALS AND ATOMS Volume: 219 Pages: 444-449, 2004
9. A CURVED DETECTION SLIT TO IMPROVE ERD ENERGY AND DEPTH RESOLUTION, BRICE DK; DOYLE BL, NUCLEAR INSTRUMENTS & METHODS IN PHYSICS RESEARCH SECTION B-BEAM INTERACTIONS WITH MATERIALS AND ATOMS Volume: 45 Issue: 1-4 Pages: 265-269, 1990.
10. THE ANALYSIS OF ELASTIC RECOIL DETECTION DATA, DOYLE BL; BRICE DK, NUCLEAR INSTRUMENTS & METHODS IN PHYSICS RESEARCH SECTION B-BEAM INTERACTIONS WITH MATERIALS AND ATOMS Volume: 35 Issue: 3-4 Pages: 301-308, 1988.
11. IBANDL: http://www-nds.iaea.org/exfor/ibandl.htm

DISTRIBUTION

Qty.	Mail Stop	Name	Org.
1	MS0747	Veena Tikare	6225 (electronic copy)
1	MS0747	Remi Dingreville	6233 (electronic copy)
1	MS0888	David Enos	1818 (electronic copy)
1	MS1056	Barney Doyle	1111 (electronic copy)
1	MS1056	Khalid Hattar	1111 (electronic copy)
1	MS1056	Jon Custer	1111 (electronic copy)
1	MS1077	David Sandison	1740 (electronic copy)
1	MS1415	Rick McCormick	1110 (electronic copy)
5	MS1423	Blythe G. Clark	1111
1	MS6231	Ruth Weiner	6231 (electronic copy)
1	MS0899	Technical Library	9536 (electronic copy)
1	MS0359	D. Chavez, LDRD Office	1911


Sandia National Laboratories